Computational Mechanics 22 (1998) 289–307 © Springer-Verlag 1998

A Lagrangian reproducing kernel particle method for metal forming analysis

J.-S. Chen, C. Pan, C. M. O. L. Roque, H.-P. Wang

Abstract A Meshless approach based on a Reproducing Kernel Particle Method is developed for metal forming analysis. In this approach, the displacement shape functions are constructed using the reproducing kernel approximation that satisfies consistency conditions. The variational equation of materials with loading-path dependent behavior and contact conditions is formulated with reference to the current configuration. A Lagrangian kernel function, and its corresponding reproducing kernel shape function, are constructed using material coordinates for the Lagrangian discretization of the variational equation. The spatial derivatives of the Lagrangian reproducing kernel shape functions involved in the stress computation of path-dependent materials are performed by an inverse mapping that requires the inversion of the deformation gradient. A collocation formulation is used in the discretization of the boundary integral of the contact constraint equations formulated by a penalty method. By the use of a transformation method, the contact constraints are imposed directly on the contact nodes, and consequently the contact forces and their associated stiffness matrices are formulated at the nodal coordinate. Numerical examples are given to verify the accuracy of the proposed meshless method for metal forming analysis.

1 Introduction

The finite element formulations of metal forming processes can be classified into three categories: the Lagrangian formulation, the Eulerian formulation, and the Arbitrary Lagrangian Eulerian (ALE) formulation. The Lagrangian formulation employs a solid mechanics approach for metal forming processes, and the method is more effective for sheet metal forming processes [Wifi et al. (1976), Wang and Budiansky (1978), Oh and Kobayashi (1980), Nakamachi et al. (1988), and Keck et al. (1990)]. For rolling and extrusion typed metal forming problems, the Lagrangian approach becomes ineffective due to severe mesh distortion. Eulerian methods have been proposed to resolve the mesh distortion difficulty [Zienkiewicz et al. (1974, 1984), Dawson (1978), and Hwu and Lenard (1988)]. The alternative ALE approaches combine the advantages of Lagrangian and Eulerian methods [Donea et al. (1977), Belytschko et al. (1978), Liu et al. (1988, 1991, 1992), Hu et al. (1993), Haber and Hariandja (1985), Ghosh and Kikuchi (1988), and Benson (1989)]. However, several drawbacks still exist in the ALE formulation. For example, controlling the mesh motion in an ALE computation to minimize the convective transport effect and the mesh distortion is tedious; especially when dealing with complex geometries. The numerical treatment of the convective transport effect also requires an additional effort.

The earliest and simplest approximation method developed for meshless computation is the kernel estimate (KE) employed in the Smooth Particle Hydrodynamics (SPH) [Lucy (1977), Monaghan (1982, 1988), Randles and Libersky (1996)]. In KE, the kernel function is normalized to assure the zero-th order consistency condition, and the use of the symmetric kernel function meets the first order consistency. However, the discretization of KE assures neither zero-th nor the first order consistency in a finite domain, unless the lumped mass (or lumped volume) is carefully selected, which is difficult to accomplish with the irregular boundary shape and arbitrary particle distribution. The first detailed investigation of the accuracy and convergence properties of meshless methods for structural analysis was due to Nayroles et al. (1992) and Belytschko et al. (1994). The Element Free Galerkin (EFG) method proposed by Belytschko et al. (1994) is based on a Moving Least-Squares approximation [Lancaster (1981)]. EFG was successfully applied to the simulation of crack propagation [Belytschko et al. (1994, 1995, 1996a, 1996b), Lu et al. (1994)]. A Reproducing Kernel Particle Method (RKPM) was introduced by Liu et al. (1995a, 1995b) to improve the accuracy of the SPH method for finite domain problems. Duarte and Oden (1995, 1996) developed the HP Cloud method for hp-adaptivity based on the Partition of Unity Method (PUM) [Melenk and Babuska (1996), Babuska and

Communicated by W-K. Liu, 7 March 1998

Jiun-Shyan Chen, Hui-Ping Wang
Department of Mechanical Engineering & Center for Computer-Aided Design, The University of Iowa, 2133 Engineering Building, Iowa City, IA 52242-1527

C.M.O.L. Roque
Department of Mechanical Engineering, State University of Campinas, SP, 13083-970, Caixa Postal 6122, Brazil

C. Pan
Peoria Proving Ground, Caterpillar Inc., Peoria, IL 61656-1895

Correspondence to: J.-S. Chen

The support of this research by National Science Foundation and Army TARDEC to the University of Iowa is greatly acknowledged.

Melenk (1996)]. In these meshless methods, the domain of interest is discretized by a set of points that are not interconnected by the structured mesh. The domain partitioning can be made independent of the nodal distributions if the Gauss integration method is used to perform domain integration. A very detailed and comprehensive overview of meshless methods can be found in Belytschko et al. (1996b).

The essential idea of RKPM [Liu et al. (1995a, 1995c, 1996a)] was to restore the discrete consistency in SPH. In this approach, a reproducing kernel (RK) approximation is introduced to impose a consistency condition to a desired order. In the continuous form of RK approximation, the imposition of the zero-th order consistency, through the correction function, is in fact equivalent to the normalization of kernel function in KE. The higher order consistency in RK approximation is achieved by the enrichment of the local polynomial basis functions to meet the completeness requirement. Through this development, the discrete consistency can be accomplished easily by a proper discretization of the moment matrix involved in the construction of the correction function. The D'Alembert's principle was recently introduced to impose essential boundary conditions [Günther et al. (1997)]. The later development of RKPM [Liu et al. (1995b, 1996b, 1996c, 1996d) and Li et al. (1996, 1997a, 1997b)] further introduced the wavelet function into RKPM formulation to construct a multiple-scale hierarchy for multiple-resolution analysis. By choosing different combinations in the wavelet series expansion, the desirable synchronized convergence properties in the interpolation can be achieved. Recent work by Li et al. (1997b) introduced a fairly simple procedure to construct a cluster of wavelet functions using the differential consistency conditions.

Chen et al. (1996, 1997a–c, 1998) extended RKPM to large deformation analysis, and demonstrated that the method is effective in dealing with large material distortion. A Lagrangian RK shape function was introduced to approximate the field variables in hyperelastic problems, formulated by the total Lagrangian formulation [Chen et al. (1997a)], and in elasto-plasticity problems formulated by the updated Lagrangian formulation [Chen et al. (1996)]. A transformation method was introduced to deal with the essential boundary conditions. With the employment of the Lagrangian RK shape function, the transformation matrix can be formed at a pre-processing stage. A nodal lumped mass was formed using the consistency condition of the transformed RK shape functions. Chen et al. (1996, 1997a) also observed that RKPM requires the use of a large kernel support to obtain an accurate solution in incompressible problems. They then proposed a pressure projection procedure [Chen et al. (1997b)] to resolve volumetric locking without the need of employing large kernel support to enhance computational efficiency and accuracy of RKPM. The method also eliminates the pressure oscillation induced from the RKPM analysis of incompressible problems. Grindeanu et al. (1996, 1997) applied RKPM to design sensitivity and optimization of hyperelastic solids.

In this paper, we employ RK approximation to formulate the discrete nonlinear equilibrium equations, and frictional contact conditions, with specific application to the metal forming problems. In Sect. 2, the basic theory of RKPM is reviewed. The Lagrangian formulation of RKPM for path-dependent materials is discussed in Sect. 3. The treatment of contact constraints in a meshless formulation is presented in Sect. 4. Section 5 gives numerical study of the solution accuracy and demonstrates the applicability of RKPM for metal forming analysis. Finally, the conclusions are outlined in Sect. 6.

2
Reproducing kernel approximation

2.1
Kernel estimate

The earliest development of the meshless methods is the Smooth Particle Hydrodynamics (SPH) [Lucy (1977), Monaghan (1982, 1988)] based on kernel estimate. The kernel estimate of a function f is an integral transformation through a kernel function Φ_a which has a compact support, as measured by a parameter a, in the following form:

$$f^k(\mathbf{x}) = \int_\Omega \Phi_a(\mathbf{x}-\mathbf{y}) f(\mathbf{y}) \mathrm{d}y \tag{2.1}$$

where f^k is the kernel estimate of f. The discrete kernel estimate is

$$f^k(\mathbf{x}) = \sum_{I=1}^{N} \Phi_a(\mathbf{x}-\mathbf{x}_I) f(\mathbf{x}_I) \Delta V_I \tag{2.2}$$

In SPH, a lumped mass $\widehat{m}_I$ is assigned to the particle I and Eq. (2.2) is usually written as:

$$f^k(\mathbf{x}) = \sum_{I=1}^{N} \Phi_a(\mathbf{x}-\mathbf{x}_I) f(\mathbf{x}_I) \frac{\widehat{m}_I}{\rho(\mathbf{x}_I)} \tag{2.3}$$

where $\rho(\mathbf{x}_I)$ is the density at particle I. If one considers $f = \rho$, then Eq. (2.3) becomes

$$\rho^k(\mathbf{x}) = \sum_{J=1}^{N} \Phi_a(\mathbf{x}-\mathbf{x}_J) \widehat{m}_J \tag{2.4}$$

As recently reported by Randles and Libersky (1996), using Eq. (2.4) for the calculation of density leads to a greater accuracy. By introducing Eq. (2.4) to Eq. (2.3), one obtains the following kernel estimate:

$$f^k(\mathbf{x}) \cong \sum_{I=1}^{N} \Phi_a(\mathbf{x}-\mathbf{x}_I) \frac{\widehat{m}_I}{\left[\sum_{J=1}^{N} \widehat{m}_J \Phi_a(\mathbf{x}_I-\mathbf{x}_J)\right]} f(\mathbf{x}_I) \tag{2.5}$$

Unfortunately, the kernel estimate of Eq. (2.5) does not exactly reproduce a unity, i.e., if $f = 1$,

$$f^k(\mathbf{x}) \cong \sum_{I=1}^{N} \left[\frac{\widehat{m}_I \Phi_a(\mathbf{x}-\mathbf{x}_I)}{\sum_{J=1}^{N} \widehat{m}_J \Phi_a(\mathbf{x}_I-\mathbf{x}_J)}\right] \neq 1 \tag{2.6}$$

Belytschko et al. (1996a) also showed that in a one-dimensional case, the discretized equation (Eq. (2.2)) does not reproduce a unity for a non-uniform arrangement of nodes. This leads to a violation of zero-th order consis-

tency condition, or the partition of unity, and therefore the convergence of the solution is not guaranteed.

2.2 Continuous reproducing kernel approximation

Liu et al. (1995a, 1995c) investigated the reproducibility of kernel estimate using a Taylor series expansion of the function f. Consider here a one-dimensional kernel estimate for simplicity, and let

$$f(y) = \sum_{n=0}^{\infty} \frac{(y-x)^n}{n!} f^{(n)}(x) \tag{2.7}$$

where $f^{(n)} = \mathrm{d}^n f / \mathrm{d}x^n$. Substituting Eq. (2.7) into the kernel estimate Eq. (2.1) yields

$$f^k(x) = m_0(x) f(x) + \sum_{n=1}^{\infty} \frac{(-1)^n}{n!} m_n(x) f^{(n)}(x) \tag{2.8}$$

where $m_n(x)$ is the moment defined by

$$m_n(x) = \int_{\Omega} (x-y)^n \Phi_a(x-y) \mathrm{d}y \tag{2.9}$$

To exactly reproduce a unity, letting $f(x) = 1$ in Eq. (2.8) leads to the following requirement:

$$m_0(x) = \int_{\Omega} \Phi_a(x-y) \mathrm{d}y = 1 \tag{2.10}$$

Equation (2.10) corresponds to the continuous form of the zero-th order consistency condition. One can also show that for the kernel estimate to reproduce a linear function $f(x) = a_0 + a_1 x$, the kernel function needs to satisfy the following conditions:

$$\begin{cases} m_0(x) = \displaystyle\int_{\Omega} \Phi_a(x-y) \mathrm{d}y = 1 \\ m_1(x) = \displaystyle\int_{\Omega} (x-y) \Phi_a(x-y) \mathrm{d}y = 0 \end{cases} \tag{2.11}$$

Consequently, in order for the kernel estimate to exactly reproduce an N-th order polynomial, the following conditions are required:

$$\begin{cases} m_0(x) = \displaystyle\int_{\Omega} \Phi_a(x-y) \mathrm{d}y = 1 \\ m_1(x) = \displaystyle\int_{\Omega} (x-y) \Phi_a(x-y) \mathrm{d}y = 0 \\ \qquad\qquad \vdots \\ m_N(x) = \displaystyle\int_{\Omega} (x-y)^N \Phi_a(x-y) \mathrm{d}y = 0 \end{cases} \tag{2.12}$$

Liu et al. (1995b) called Eq. (2.12) the reproducing conditions. It is noted that Eq. (2.12) leads to the following conditions:

$$\begin{cases} \displaystyle\int_{\Omega} \Phi_a(x-y) \mathrm{d}y = 1 \\ \displaystyle\int_{\Omega} y \Phi_a(x-y) \mathrm{d}y = x \\ \qquad\qquad \vdots \\ \displaystyle\int_{\Omega} y^N \Phi_a(x-y) \mathrm{d}y = x^N \end{cases} \tag{2.13}$$

In fact, a zero-th consistency condition (Eq. (2.10)) can be easily satisfied by the normalization of the kernel function. However, the higher-order consistency conditions are difficult to meet, and most of the kernel functions do not satisfy these reproducing conditions. To formulate the reproducing kernel approximation, we rewrite Eq. (2.12) in the following form:

$$\int_{\Omega} \mathbf{H}(x-y) \Phi_a(x-y) \mathrm{d}y = \mathbf{H}(0) \tag{2.14}$$

$$\mathbf{H}^{\mathrm{T}}(x-y) = \left[1, x-y, \ldots, (x-y)^N\right] \tag{2.15}$$

Liu et al. (1995a, 1995c) proposed a reproducing kernel approximation by introducing a correction function to the kernel estimate:

$$f^R(x) = \int_{\Omega} C(x; x-y) \Phi_a(x-y) f(y) \mathrm{d}y \tag{2.16}$$

where $f^R(x)$ is the "reproduced" function of $f(x)$, and Eq. (2.16) is the reproducing kernel approximation, or the reproducing equation. The function $C(x; x-y)$ is the correction function defined by

$$C(x; x-y) = b_0(x) + b_1(x)(x-y) + \cdots + b_N(x)(x-y)^N = \mathbf{b}^{\mathrm{T}}(x) \mathbf{H}(x-y) \tag{2.17}$$

$$\mathbf{b}^{\mathrm{T}}(x) = [b_0(x), b_1(x), \ldots, b_N(x)] \tag{2.18}$$

and $b_i(x)$'s are determined by the satisfaction of the reproducing conditions, i.e.,

$$\int_{\Omega} C(x; x-y) \Phi_a(x-y) \mathbf{H}(x-y) \mathrm{d}y = \mathbf{H}(0) \tag{2.19}$$

Substituting Eq. (2.17) into Eq. (2.19) leads to

$$\left[\int_{\Omega} \mathbf{H}(x-y) \Phi_a(x-y) \mathbf{H}^{\mathrm{T}}(x-y) \mathrm{d}y\right] \mathbf{b}(x) = \mathbf{H}(0) \tag{2.20}$$

and the unknown vector $\mathbf{b}(x)$ is solved by

$$\mathbf{b}(x) = \mathbf{M}(x)^{-1} \mathbf{H}(0) \tag{2.21}$$

$$\mathbf{M}(x) = \int_{\Omega} \mathbf{H}(x-y) \mathbf{H}^{\mathrm{T}}(x-y) \Phi_a(x-y) \mathrm{d}y \tag{2.22}$$

Introducing Eqs. (2.17) and (2.21) into Eq. (2.16) results in the following reproducing kernel approximation:

$$f^R(x) = \int_{\Omega} C(x; x-y) \Phi_a(x-y) f(y) \mathrm{d}y = \mathbf{H}^{\mathrm{T}}(0) \mathbf{M}^{-1}(x) \int_{\Omega} \mathbf{H}(x-y) \Phi_a(x-y) f(y) \mathrm{d}y \tag{2.23}$$

A multi-dimensional extension of Eq. (2.23) is straightforward, simply by setting $x \to \mathbf{x} \equiv [x_1, x_2, x_3]$, $y \to \mathbf{y} \equiv [y_1, y_2, y_3]$, and $\mathrm{d}y \to \mathrm{d}\Omega_y \equiv \mathrm{d}y_1\, \mathrm{d}y_2\, \mathrm{d}y_3$, $\Phi_a(x-y) \to \Phi_a(\mathbf{x}-\mathbf{y})$, and letting $\mathbf{H}$ be a vector of monomial basis functions,

$$\mathbf{H}^{\mathrm{T}}(x-y)=[1,x_1-y_1,x_2-y_2,x_3 -y_3,(x_1-y_1)^2,\ldots,(x_3-y_3)^N]\ , \quad (2.24)$$

Equation (2.23) can be recast into the following form,

$$f^R(\mathbf{x})=\int_\Omega \bar{\Phi}_a(\mathbf{x};\mathbf{x}-\mathbf{y})f(\mathbf{y})\mathrm{d}\Omega_y \quad (2.25)$$

where $\bar{\Phi}_a(\mathbf{x};\mathbf{x}-\mathbf{y})=C(\mathbf{x};\mathbf{x}-\mathbf{y})\Phi_a(\mathbf{x}-\mathbf{y})$ is called the reproduced kernel, and $\Phi_a(x-y)$ is the multi-dimensional kernel function. Since Eq. (2.25) exactly reproduces N-th order monomial, the method fulfills the N-th order consistency conditions, i.e.,

$$\int_\Omega \bar{\Phi}_a(\mathbf{x};\mathbf{x}-\mathbf{y})\, y_1^i\, y_2^j\, y_3^k\, \mathrm{d}\Omega_y = x_1^i\, x_2^j\, x_3^k, \quad i+j+k=0,\ldots,N \quad (2.26)$$

2.3 Discrete reproducing kernel approximation

To construct an approximation function for a finite dimensional solution of the partial differential equations, the domain Ω is discretized by a set of nodes $\{\mathbf{x}_I,\ldots,\mathbf{x}_{\mathrm{NP}}\}$, where $\mathbf{x}_I$ is the position vector of node I, and NP is the total number of points (nodes). By performing nodal integration with unit weights of Eq. (2.23), the continuous reproducing equation is discretized into

$$f^h(\mathbf{x})=\sum_{I=1}^{\mathrm{NP}} C(\mathbf{x};\mathbf{x}-\mathbf{x}_I)\Phi_a(x-\mathbf{x}_I)f_I \equiv \sum_{I=1}^{NP}\Psi_I(\mathbf{x})f_I \quad (2.27)$$

where

$$\Psi_I(\mathbf{x})=C(\mathbf{x};\mathbf{x}-\mathbf{x}_I)\Phi_a(\mathbf{x}-\mathbf{x}_I) \quad (2.28)$$

$$C(\mathbf{x};\mathbf{x}-\mathbf{x}_I)=\mathbf{H}^{\mathrm{T}}(\mathbf{0})\mathbf{M}^{-1}(\mathbf{x})\mathbf{H}(\mathbf{x}-\mathbf{x}_I) \quad (2.29)$$

where $\Psi_I(\mathbf{x})$ and f_I are the shape function and the corresponding coefficient of the reproducing kernel approximation. Note that since $\Psi_I(\mathbf{x}_J)\neq\delta_{IJ}$, and the coefficient f_I is not the nodal value of $f^h(\mathbf{x})$, i.e., $f_I\neq f^h(\mathbf{x}_I)$. Using Eqs. (2.28) and (2.29) one can obtain the derivative of $\Psi_I(x)$ as

$$\Psi_{I,i}(\mathbf{x})=\mathbf{H}^{\mathrm{T}}(\mathbf{0})\Big[\mathbf{M}^{-1}_{,i}(\mathbf{x})\mathbf{H}(\mathbf{x}-\mathbf{x}_I)\Phi_a(\mathbf{x}-\mathbf{x}_I) + \mathbf{M}^{-1}(\mathbf{x})\mathbf{H}_{,i}(\mathbf{x}-\mathbf{x}_I)\Phi_a(\mathbf{x}-\mathbf{x}_I) + \mathbf{M}^{-1}(\mathbf{x})\mathbf{H}(\mathbf{x}-\mathbf{x}_I)\Phi_{a,i}(\mathbf{x}-\mathbf{x}_I)\Big] \quad (2.30)$$

where $(\ )_{,i}\equiv\frac{\partial(\ )}{\partial x_i}$ and $\mathbf{M}^{-1}_{,i}$ is computed by $\mathbf{M}^{-1}_{,i}(x)=-\mathbf{M}(x)^{-1}\mathbf{M}(x)_{,i}\mathbf{M}(x)^{-1}$. As discussed in Chen et al. (1996), in order to preserve the consistency condition in a discretized reproducing equation, Eq. (2.27), the moment matrix $\mathbf{M}(\mathbf{x})$ needs to be discretized with the same discretization method as was used in the Reproducing equation, i.e.,

$$\mathbf{M}(\mathbf{x})=\sum_{I=1}^{\mathrm{NP}}\mathbf{H}(\mathbf{x}-\mathbf{x}_I)\mathbf{H}^{\mathrm{T}}(\mathbf{x}-\mathbf{x}_I)\Phi_a(\mathbf{x}-\mathbf{x}_I) \quad (2.31)$$

For example, the reproducing kernel shape function corresponding to a constant basis function $\mathbf{H}=[1]$ is:

$$\mathbf{M}(x)=\sum_{I=1}^{\mathrm{NP}}\Phi_a(\mathbf{x}-\mathbf{x}_I)\rightarrow\Psi_I(\mathbf{x})=\frac{\Phi_a(\mathbf{x}-\mathbf{x}_I)}{\sum_{J=1}^{\mathrm{NP}}\Phi_a(\mathbf{x}-\mathbf{x}_J)} \quad (2.32)$$

Equation (2.32) is called the Shepard function that satisfies:

$$\sum_{I=1}^{\mathrm{NP}}\Psi_I(\mathbf{x})=1 \quad (2.33)$$

Equation (2.33) corresponds to Eq. (2.27) with $f(x)=1$, which is the zero-th consistency condition, or the Partition of Unity. For a general consideration of N-th order monomial basis function, one can show that:

$$\begin{aligned}\sum_{I=1}^{\mathrm{NP}}&\Psi_I(\mathbf{x})\mathbf{H}^{\mathrm{T}}(\mathbf{x}-\mathbf{x}_I)\\ &=\sum_{I=1}^{\mathrm{NP}}\big[\mathbf{H}^{\mathrm{T}}(\mathbf{0})\mathbf{M}^{-1}(\mathbf{x})\mathbf{H}(\mathbf{x}-\mathbf{x}_I)\\ &\quad\times\Phi_a(\mathbf{x}-\mathbf{x}_I)\mathbf{H}^{\mathrm{T}}(\mathbf{x}-\mathbf{x}_I)\big]\\ &=\mathbf{H}^T(\mathbf{0})\end{aligned} \quad (2.34)$$

and Eq. (2.34) leads to the N-th order consistency condition:

$$\sum_{I=1}^{\mathrm{NP}}\Psi_I(\mathbf{x})\mathbf{H}^{\mathrm{T}}(\mathbf{x}_I)=\mathbf{H}^{\mathrm{T}}(\mathbf{x}) \quad (2.35)$$

or

$$\sum_{I=1}^{\mathrm{NP}}\Psi_I(\mathbf{x})x_{1I}^i\,x_{2I}^j\,x_{3I}^k=x_1^i\,x_2^j\,x_3^k, \quad i+j+k=0,\ldots,N \quad (2.36)$$

To compute $\Psi_{I,i}(\mathbf{x})$, the term $\mathbf{M}(\mathbf{x})_{,i}$ also needs to be formed numerically. The differentiation of Eq. (2.31) leads to

$$\begin{aligned}\mathbf{M}_{,i}=\sum_{I=1}^{\mathrm{NP}}\big[&\mathbf{H}_{,i}(\mathbf{x}-\mathbf{x}_I)\mathbf{H}^{\mathrm{T}}(\mathbf{x}-\mathbf{x}_I)\Phi_a(\mathbf{x}-\mathbf{x}_I)\\ &+\mathbf{H}(\mathbf{x}-\mathbf{x}_I)\mathbf{H}^{\mathrm{T}}_{,i}(\mathbf{x}-\mathbf{x}_I)\Phi_a(\mathbf{x}-\mathbf{x}_I)\\ &+\mathbf{H}(\mathbf{x}-\mathbf{x}_I)\mathbf{H}^{\mathrm{T}}(\mathbf{x}-\mathbf{x}_I)\Phi_{a,i}(\mathbf{x}-\mathbf{x}_I)\big]\end{aligned} \quad (2.37)$$

The use of Eq. (2.37) in Eq. (2.30) yields the following differential consistency condition:

$$\sum_{I=1}^{\mathrm{NP}}\Psi_{I,i}(\mathbf{x})\mathbf{H}^{\mathrm{T}}(\mathbf{x}_I)=\mathbf{H}^{\mathrm{T}}_{,i}(\mathbf{x}) \quad (2.38)$$

Figure 1(a) illustrates that the KE shape functions (Eq. (2.28) without correction function) do not satisfy the constant consistency condition (or Partition of Unity) near the boundaries, and particle refinement reduces the error near the boundaries. Similarly, the KE shape functions do not satisfy the x-linear consistency condition near the boundaries, and the boundary errors can be reduced by a particle refinement as shown in Fig. 1(b). As expected, RK shape functions satisfy constant and x-linear consistency

conditions using the linear basis functions $\mathbf{H}^{\mathrm{T}} = [1, x]$. Similarly, KE shape functions do not meet the differential consistency conditions near the boundaries, whereas RK shape functions exactly satisfy differential consistencies as shown in Figs. (2a) and (2b).

3
Lagrangian reproducing kernel formulation for elasto-plasticity

3.1
Governing equations

In a Lagrangian (or material) formulation, we follow the motion of all the material particles in the body from its original configuration Ω_X with the boundary Γ_X, to the current configuration Ω_x with the boundary Γ_x. The motion of a material particle originally located at a position $\mathbf{X} \in \Omega_X$ is described by a mapping $\mathbf{x} = \boldsymbol{\varphi}(\mathbf{X}, t)$ $(x_i = \varphi_i(\mathbf{X}, t))$, where $\boldsymbol{x} \in \Omega_x$ is the spatial location of the material particle $\mathbf{X}$ at time t, and φ_i is the mapping function. For loading path-dependent material behavior, the constitutive equations are expressed in the current configuration, and therefore it is more convenient to reference the kinematic and kinetic variables to the current configuration in the variational equation (updated Lagrangian formulation). In Lagrangian formulation, the primary unknown variable is the *material* displacement which is defined by

$$\mathbf{u}(\mathbf{X}, t) = \varphi(\mathbf{X}, t) - \mathbf{X} \tag{3.1}$$

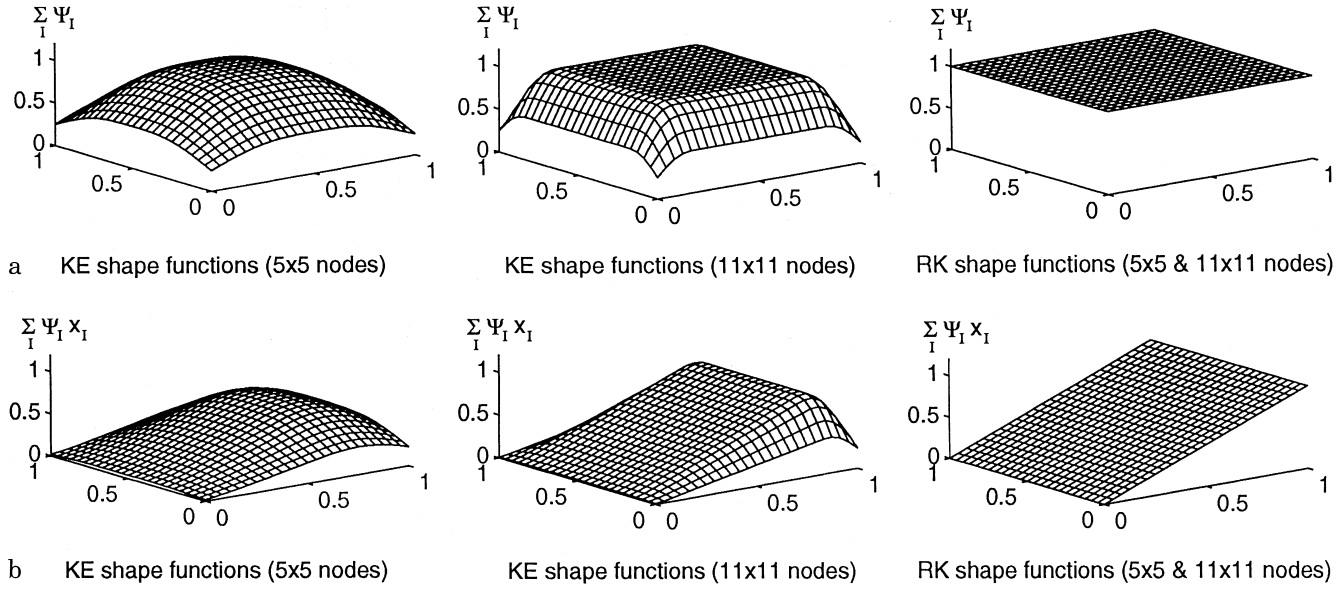

Fig. 1a,b. Constant and linear consistency conditions of KE and RK shape functions

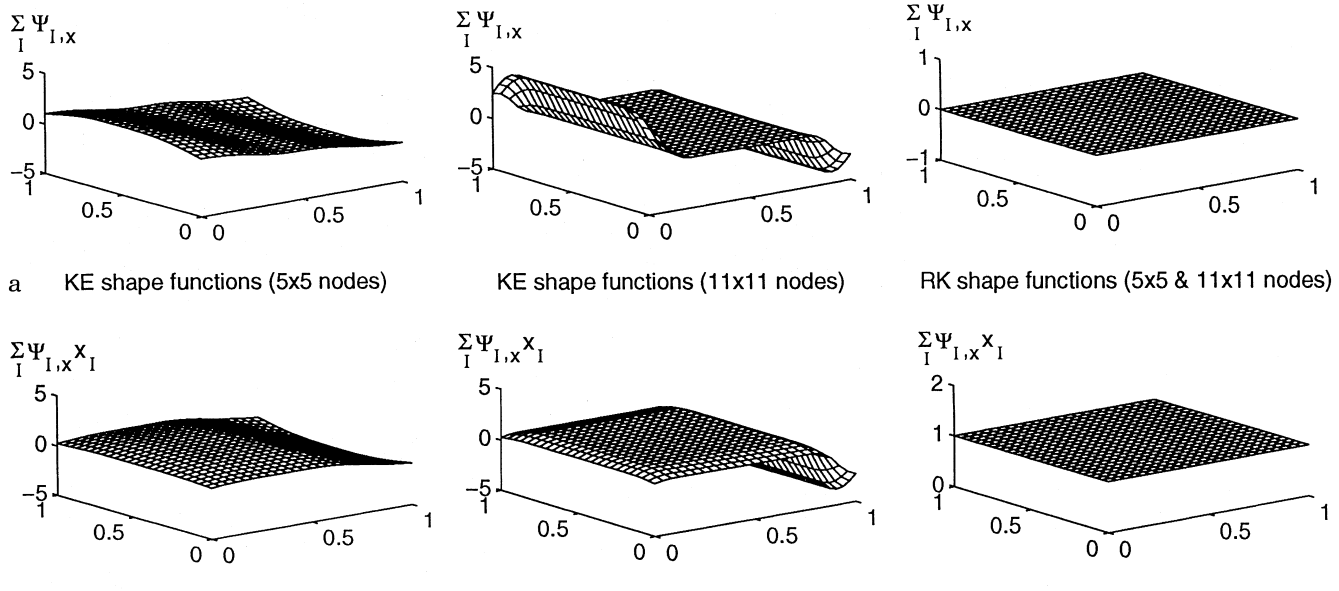

Fig. 2a,b. Differential consistency conditions of KE and RK shape functions

Note that Eq. (3.1) is the measure of displacement following a fixed material point **X**. This identification of material displacement is important since the later development of reproducing kernel shape functions for displacements will be based on the material coordinates (material quantity). Consequently, the material velocity v and material acceleration a are defined by

$$v(\mathbf{X},t)=\left.\frac{\partial\varphi(\mathbf{X},t)}{\partial t}\right|_{[\mathbf{X}]}=\left.\frac{\partial\mathbf{u}(\mathbf{X},t)}{\partial t}\right|_{[\mathbf{X}]}\equiv\dot{\mathbf{u}}(\mathbf{X},t) \tag{3.2}$$

$$a(\mathbf{X},t)=\left.\frac{\partial^2\varphi(\mathbf{X},t)}{\partial t^2}\right|_{[\mathbf{X}]}=\left.\frac{\partial^2\mathbf{u}(\mathbf{X},t)}{\partial t^2}\right|_{[\mathbf{X}]}\equiv\ddot{\mathbf{u}}(\mathbf{X},t) \tag{3.3}$$

The statement of variational equation is then given as the following: Given the body force b_i in the domain Ω_x, the surface traction h_i on the natural boundary $\Gamma_x^{h_i}$, the prescribed boundary displacement g_i on the essential boundary $\Gamma_x^{g_i}$, the initial displacement u_i^0 and the initial velocity v_i^0 in the domain Ω_X, find $u_i\in\mathbf{H}_g^1(\mathbf{H}_g^1=\{\mathbf{u}:\mathbf{u}\in\mathbf{H}^1,u_i=g_i \text{ on } \Gamma_x^{g_i}\})$, such that for all $\delta u_i\in\mathbf{H}_0^1$ $(\mathbf{H}_0^1=\{w:w\in\mathbf{H}^1, w_i=0 \text{ on } \Gamma_x^{g_i}\})$, the following equation is satisfied [Atluri, (1980)]:

$$\delta\Pi=\int_{\Omega_x}\delta u_i\rho\ddot{u}_i\,\mathrm{d}\Omega+\int_{\Omega_x}\delta u_{i,j}\tau_{ij}\,\mathrm{d}\Omega-\int_{\Omega_x}\delta u_i b_i\,\mathrm{d}\Omega-\int_{\Gamma_x^{h_x}}\delta u_i h_i\,\mathrm{d}\Gamma=0 \tag{3.4}$$

with initial conditions

$$u_i(\mathbf{X},0)=u_i^0(\mathbf{X}) \tag{3.5}$$

$$\dot{u}_i(\mathbf{X},0)=v_i^0(\mathbf{X}) \tag{3.6}$$

where $\mathbf{H}^1$ is the Sobolev space of degree one, $(\,)_{,i}\equiv\partial(\,)/\partial x_i$ denotes the spatial derivative, and τ_{ij} is the Cauchy stress obtained from constitutive equations. Equation (3.4) is a Lagrangian description formulated in the current configuration. It should be realized that in the Lagrangian description the "current" integration domain Ω_x and boundary Γ_x moves with the material particles and are not fixed in space. Consequently the Cauchy stress is evaluated at a spatial coordinate $x=\varphi(\mathbf{X},t)$ of a *fixed* particle **X**, and therefore the stress update is processed with respect to the same material particle in the Lagrangian setting.

The linearization of Eq. (3.4) requires the employment of stress rate. Many frame indifference stress rates can be used [Atluri (1984)], and the linearized equation, in general, can be written in the following form [see Atluri (1980) and Atluri and Cazzani (1994) for details]:

$$\Delta\delta\Pi=\int_{\Omega_x}\delta u_i\rho\Delta\ddot{u}_i\,\mathrm{d}\Omega+\int_{\Omega_x}\delta u_{i,j}(\mathbf{D}_{ijkl}+\mathbf{T}_{ijkl})\Delta u_{k,l}\,\mathrm{d}\Omega-\int_{\Omega_x}\delta u_i\Delta b_i\,\mathrm{d}\Omega-\int_{\Gamma_x^{h_i}}\delta u_i\Delta h_i\,\mathrm{d}\Gamma \tag{3.7}$$

where $\mathbf{D}_{ijkl}$ and $\mathbf{T}_{ijkl}$ are the material response and the geometric response (initial stress) tensors that are closely related to the stress rate employed in the linearization of Cauchy stress. For example, if Jaumann stress rate is used

$$\mathbf{D}_{ijkl}=\mathbf{C}^c_{ijkl} \tag{3.8a}$$

$$\mathbf{T}_{ijkl}=\tau_{ij}\delta_{kl}-\tfrac{1}{2}\tau_{il}\delta_{ik}+\tfrac{1}{2}\tau_{jl}\delta_{ik}-\tfrac{1}{2}\tau_{ik}\delta_{jl}-\tfrac{1}{2}\tau_{jk}\delta_{il} \tag{3.8b}$$

and $\mathbf{C}^c_{ijkl}$ is the constitutive tensor that relates Jaumann stress rate to velocity strain. Whereas if Truesdell stress rate is used,

$$\mathbf{D}_{ijkl}=\mathbf{C}^{\mathrm{t}}_{ijkl} \tag{3.9a}$$

$$\mathbf{T}_{ijkl}=\tau_{jk}\delta_{il} \tag{3.9b}$$

where $\mathbf{C}^{\mathrm{t}}_{ijkl}$ is the constitutive tensor that relates Truesdell stress rate to velocity strain. The incrementally objective algorithm proposed by Hughes and Winget (1980), Rubinstein and Atluri (1983), and Reed and Atluri (1985) can be used to integrate the elastic response of Cauchy stress due to rotational effect, and the algorithmic tangent operator consistent to the return mapping algorithm presented by Simo et al. (1985) is employed to form the elasto-plastic material response tensor. Alternatively, if the yield surface is an isotropic function, Simo et al. (1988) established a hyperelastic-based stress-strain relation (total form) for stress and internal variable computations based on the principle of maximum plastic dissipation and the multiplicative decomposition of deformation gradient. The consistent tangent operator of this approach formulated by Simo et al. (1988, 1992) should be used in the incremental equation to ensure the quadratic rate of convergence.

3.2 Lagrangian and Eulerian reproducing kernel shape functions

To describe the motion of a body, one can consider a material description of a kinematic variable $G^X(\mathbf{X},t)$, or its spatial description $G^x(\mathbf{x},t)=G^X(\mathbf{X},t)$ where $\boldsymbol{x}=\boldsymbol{\varphi}(\mathbf{X},t)$. Choosing one over another depends entirely on the selection of a reference configuration. The material time derivative of $G^X(\mathbf{X},t)$ is

$$\left.\frac{\partial G^X(\mathbf{X},t)}{\partial t}\right|_{[\mathbf{X}]}=\left.\frac{\partial G^x(\mathbf{x},t)}{\partial t}\right|_{[\mathbf{x}]}+v^x\cdot(\nabla G^x(\mathbf{x},t))\equiv\frac{DG^x(\mathbf{x},t)}{Dt} \tag{3.10}$$

where $\boldsymbol{v}^X(\mathbf{X},t)=\boldsymbol{v}^X(\mathbf{X},t)$ is the spatial description of the material velocity $\boldsymbol{v}^X(\mathbf{X},t)$ with $\mathbf{x}=\varphi(\mathbf{X},t)$ (the *material* velocity defined in Eq. (3.2) is denoted here more precisely by $\boldsymbol{v}^X(\mathbf{X},t)$). Consequently, the material acceleration is defined by the material time derivative of the material velocity

$$a_i^X(\mathbf{X},t)=\left.\frac{\partial v_i^X(\mathbf{X},t)}{\partial t}\right|_{[\mathbf{X}]}=\left.\frac{\partial v_i^x(\mathbf{x},t)}{\partial t}\right|_{[\mathbf{X}]}+\frac{\partial v_i^x(\mathbf{x},t)}{\partial x_j}v_j^x\equiv\frac{Dv_i^x(\mathbf{x},t)}{Dt} \tag{3.11}$$

To introduce the reproducing kernel approximation of displacements, one can first consider a Lagrangian kernel

function expressed in a material description, Φ_a^X. Take a cubic B-spline kernel function for example:

$$\Phi_a^X(\mathbf{X}-\mathbf{X}_I)=\frac{1}{a}\begin{cases}\frac{2}{3}-4\left(\frac{\|\mathbf{X}-\mathbf{X}_I\|}{a}\right)^2+4\left(\frac{\|\mathbf{X}-\mathbf{X}_I\|}{a}\right)^3 & \text{for } 0\le\frac{\|\mathbf{X}-\mathbf{X}_I\|}{a}\le\frac{1}{2}\\ \frac{4}{3}-4\left(\frac{\|\mathbf{X}-\mathbf{X}_I\|}{a}\right)+4\left(\frac{\|\mathbf{X}-\mathbf{X}_I\|}{a}\right)^2-\frac{4}{3}\left(\frac{\|\mathbf{X}-\mathbf{X}_I\|}{a}\right)^3 & \text{for } \frac{1}{2}<\frac{\|\mathbf{X}-\mathbf{X}_I\|}{a}\le 1\\ 0 & \text{otherwise}\end{cases} \tag{3.12}$$

and the spatial description of the Lagrangian kernel function, Φ_a^x, is

$$\Phi_a^x(\mathbf{x},\mathbf{x}_I,t)=\Phi_a^X(\varphi^{-1}(\mathbf{x},t)-\varphi^{-1}(\mathbf{x}_I,t)) \tag{3.13}$$

The value of the Lagrangian kernel function is determined on the distance between *material* points $\mathbf{X}$ and $\mathbf{X}_I$. Thus the support radius of this Lagrangian kernel function a is defined in the initial configuration, and the support covers the same set of material points throughout the course of deformation. One can also consider an Eulerian kernel function expressed in a spatial description:

$$\phi_a^x(\mathbf{x}-\mathbf{x}_I)=\frac{1}{a}\begin{cases}\frac{2}{3}-4\left(\frac{\|\mathbf{x}-\mathbf{x}_I\|}{a}\right)^2+4\left(\frac{\|\mathbf{x}-\mathbf{x}_I\|}{a}\right)^3 & \text{for } 0\le\frac{\|\mathbf{x}-\mathbf{x}_I\|}{a}\le\frac{1}{2}\\ \frac{4}{3}-4\left(\frac{\|\mathbf{x}-\mathbf{x}_I\|}{a}\right)+4\left(\frac{\|\mathbf{x}-\mathbf{x}_I\|}{a}\right)^2-\frac{4}{3}\left(\frac{\|\mathbf{x}-\mathbf{x}_I\|}{a}\right)^3 & \text{for } \frac{1}{2}<\frac{\|\mathbf{x}-\mathbf{x}_I\|}{a}\le 1\\ 0 & \text{otherwise}\end{cases} \tag{3.14}$$

and the material description of this Eulerian cubic B-spline kernel function, ϕ_a^X, is

$$\phi_a^X(\mathbf{X},\mathbf{X}_I,t)=\phi_a^x(\varphi(\mathbf{X},t)-\varphi(\mathbf{X}_I,t)) \tag{3.15}$$

The value of the Eulerian kernel function is determined by the distance between *spatial* points $\mathbf{x}$ and $\mathbf{x}_I$. Thus the Eulerian kernel function has a support radius of a defined in the current configuration, and the support covers different material points at a different time t.

The next step is to construct the reproducing kernel shape function for large deformation. The material description of the Lagrangian reproducing kernel shape function, $\Psi_I^X(\mathbf{X})$, is constructed using the Lagrangian kernel function $\Phi_a^X(\mathbf{X}-\mathbf{X}_I)$ with the discrete reproducing conditions imposed at the initial configuration to yield

$$\Psi_I^X(\mathbf{X})=\mathbf{H}^{\mathrm{T}}(\mathbf{0})\mathbf{M}^{-1}(\mathbf{X})\mathbf{H}(\mathbf{X}-\mathbf{X}_I)\Phi_a^X(\mathbf{X}-\mathbf{X}_I) \tag{3.16}$$

$$\mathbf{M}(\mathbf{X})=\sum_{I=1}^{\mathrm{NP}}\mathbf{H}(\mathbf{X}-\mathbf{X}_I)\mathbf{H}^{\mathrm{T}}(\mathbf{X}-\mathbf{X}_I)\Phi_a^X(\mathbf{X}-\mathbf{X}_I) \tag{3.17}$$

$$\mathbf{H}^{\mathrm{T}}(\mathbf{X}-\mathbf{X}_I)=[1,X_1-X_{1I},X_2-X_{2I},X_3-X_{3I},\ldots,(X_3-X_{3I})^N] \tag{3.18}$$

This set of Lagrangian reproducing kernel shape functions $\{\Psi_1^X,\Psi_2^X,\ldots,\Psi_{\mathrm{NP}}^X\}$ satisfies the following consistency conditions:

$$\sum_{I=1}^{\mathrm{NP}}\Psi_I^X(\mathbf{X})\,X_{1I}^i\,X_{2I}^j\,X_{3I}^k=X_1^i\,X_2^j\,X_3^k;\qquad i+j+k=0,\ldots,N \tag{3.19}$$

Similarly, the spatial description of the Eulerian reproducing kernel shape function, $\Psi_I^x(x)$, is constructed using the Eulerian kernel function $\phi_a^x(x-x_I)$ with the discrete reproducing conditions imposed at the current configuration to yield

$$\Psi_I^x(\mathbf{x})=\mathbf{h}^{\mathrm{T}}(\mathbf{0})\mathbf{m}^{-1}(\mathbf{x})\mathbf{h}([\mathbf{x}-\mathbf{x}_I)\Phi_a^x(\mathbf{x}-\mathbf{x}_I) \tag{3.20}$$

$$\mathbf{m}(\mathbf{x})=\sum_{I=1}^{\mathrm{NP}}\mathbf{h}(\mathbf{x}-\mathbf{x}_I)\mathbf{h}^{\mathrm{T}}(\mathbf{x}-\mathbf{x}_I)\Phi_a^x(\mathbf{x}-\mathbf{x}_I) \tag{3.21}$$

$$\mathbf{h}^{\mathrm{T}}(\mathbf{x}-\mathbf{x}_I)=[1,x_1-x_{1I},x_2-x_{2I},x_3-x_{3I},\ldots,(x_3-x_{3I})^N] \tag{3.22}$$

and this set of Eulerian reproducing kernel shape functions $\{\Psi_1^x,\Psi_2^x,\ldots,\Psi_{\mathrm{NP}}^x\}$ satisfies the following consistency conditions:

$$\sum_{I=1}^{\mathrm{NP}}\Psi_I^x(\mathbf{x})\,x_{1I}^i\,x_{2I}^j\,x_{3I}^k=x_1^i\,x_2^j\,x_3^k;\qquad i+j+k=0,\ldots,N \tag{3.23}$$

In Lagrangian formulation, it is more convenient to employ the Lagrangian reproducing kernel shape functions with material description for the approximation of material displacement:

$$u_i^X(\mathbf{X},t)=\varphi_i(\mathbf{X}_i,t)-\mathbf{X}_i=\sum_{I=1}^{\mathrm{NP}}\Psi_I^X(\mathbf{X})d_{iI}(t) \tag{3.24}$$

where $d_{iI}(t)'^S$ are the time-dependent coefficients of $\Psi_I^X(\mathbf{X})'^S$, and the material velocity and material acceleration are obtained by

$$v_i^X(\mathbf{X},t)=\left.\frac{\partial u_i(\mathbf{X},t)}{\partial t}\right|_{[\mathbf{X}]}=\sum_{I=1}^{\mathrm{NP}}\Psi_I^X(\mathbf{X})\dot{d}_{iI}(t) \tag{3.25}$$

$$a_i^X(\mathbf{X},t)=\left.\frac{\partial^2 u_i^X(\mathbf{X},t)}{\partial t^2}\right|_{[\mathbf{X}]}=\sum_{I=1}^{\mathrm{NP}}\Psi_I^X(\mathbf{X})\ddot{d}_{iI}(t) \tag{3.26}$$

If an Eulerian reproducing kernel function is used for the approximation of material displacement,

$$u_i^x(\mathbf{x},t)=x_i-\varphi_i^{-1}(\mathbf{x},t)=\sum_{I=1}^{\mathrm{NP}}\Psi_I^x(\mathbf{x})\xi_{iI}(t) \tag{3.27}$$

where $\xi_{iI}(t)'^{S}$ are the time-dependent coefficients of $\Psi_I^x(x)'^{S}$, and the spatial description of the material velocity is obtained by

$$\left.\frac{\partial u_i^x(\mathbf{x},t)}{\partial t}\right|_{[\mathbf{X}]} = \left.\frac{\partial u_i^x(\mathbf{x},t)}{\partial t}\right|_{[\mathbf{x}]} + \frac{\partial u_i^x(\mathbf{x},t)}{\partial x_j} v_j^x(\mathbf{x},t)$$
$$= \sum_{I=1}^{\mathrm{NP}} \left[\Psi_I^x(\mathbf{x}) \dot{\xi}_{iI}(t) + v_j^x(\mathbf{x}) \frac{\partial \Psi_I^x(\mathbf{x})}{\partial x_j} \xi_{iI}(t) \right] \tag{3.28}$$

An additional convective term is involved in Eq. (3.28) when Eulerian reproducing kernel shape functions are used for the approximation of field variables, and this complicates the computation as compared to the use of the Lagrangian reproducing kernel shape functions. On the other hand, the updated Lagrangian formulation of the variational equation (Eq. (3.4)) requires a spatial derivatives on the displacements. Taking the spatial derivatives of the Eulerian reproducing kernel shape functions is straightforward, but taking the spatial derivatives of the Lagrangian Reproducing shape functions requires the following computation:

$$\frac{\partial \Psi_I^X(\mathbf{X})}{\partial x_i} = \frac{\partial \Psi_I^X(\mathbf{X})}{\partial X_j} \frac{\partial X_j}{\partial x_i} = \frac{\partial \Psi_I^X(\mathbf{X})}{\partial X_j} F_{ji}^{-1} \tag{3.29}$$

To avoid taking the spatial derivatives of $\Psi_I^X(\mathbf{X})$ involved in $\mathbf{F}^{-1}$, $\mathbf{F}^{-1}$ is computed indirectly by taking the inversion of $\mathbf{F}$, i.e.,

$$\mathbf{F}^{-1} = \left[\sum_{I=1}^{\mathrm{NP}} \mathbf{d}_I \otimes \frac{\partial \Psi_I^X(\mathbf{X})}{\partial \mathbf{X}} + \mathbf{I} \right]^{-1} \tag{3.30}$$

where $\mathbf{I}$ is the second order identity tensor.

3.3 Coordinate transformation and the reproducing kernel matrix equation

Since the meshless shape functions such as the reproducing kernel shape functions or Moving Least-Square shape functions do not have Kronecker delta properties, the essential boundary conditions need to be imposed by the Lagrange multiplier method [Belytschko et al. (1994), Lu et al. (1994)], or by the transformation method (Chen et al. (1996, 1997a). The first approach requires the solution of independent kinematic variables as well as Lagrange multipliers at each incremental step. Further, one needs to consider the stability condition, the Babuska-Brezzi condition [Babuska (1973), Brezzi (1974)], when more than one independent variables are used in the variational equation. The second approach transforms the generalized coordinates to nodal coordinates to allow a direct treatment of the essential boundary conditions. Since the second approach can be easily applied to contact problems (discussed in the next section), the method is used here to establish the discrete RKPM equation for general elastoplasticity problem.

Using the Lagrangian reproducing kernel shape functions, the kinematic admissible displacement $u_i^h(\mathbf{X},t)$ of the variational equation, Eq. (3.4), needs to satisfy the following conditions:

$$\left.\begin{aligned} u_i^h(\mathbf{X}_J,t) &= \sum_{I=1}^{\mathrm{NP}} \Psi_I^X(\mathbf{X}_J) d_{iI}(t) = g_i(\mathbf{X}_J,t) \\ \delta u_i^h(\mathbf{X}_J,t) &= \sum_{I=1}^{\mathrm{NP}} \Psi_I^X(\mathbf{X}_J) \delta d_{iI}(t) = 0 \end{aligned}\right\} \quad \forall J \in \eta_{g_i} \tag{3.31}$$

where η_{g_i} denotes a set of particle numbers in which the associated particles are located on $\Gamma_X^{g_i}$. Equation (3.31) represents two sets of constraint equations that are needed to be solved simultaneously, with the equation of motion. Using the transformation method, the transformation matrix is formed by establishing the relationship between the nodal value $u_i^h(X_J,t) \equiv \hat{d}_{iJ}(t)$ and the "generalized" displacement $d_{iJ}(t)$:

$$\hat{d}_{ij}(t) = \sum_{I=1}^{\mathrm{NP}} \Psi_I^X(\mathbf{X}_J) d_{iI}(t) = \sum_{I=1}^{\mathrm{NP}} L_{IJ} d_{iI}(t) \tag{3.32}$$

or

$$\begin{bmatrix} \hat{\mathbf{d}}_1 \\ \hat{\mathbf{d}}_2 \\ \vdots \\ \hat{\mathbf{d}}_N \end{bmatrix} = \underbrace{\begin{bmatrix} L_{11}\mathbf{I} & L_{21}\mathbf{I} & \cdots & L_{N1}\mathbf{I} \\ L_{12}\mathbf{I} & L_{22}\mathbf{I} & \cdots & L_{N2}\mathbf{I} \\ \vdots & \vdots & \ddots & \vdots \\ L_{1N}\mathbf{I} & L_{2N}\mathbf{I} & \cdots & L_{NN}\mathbf{I} \end{bmatrix}}_{\boldsymbol{\Lambda}^{\mathrm{T}}} \begin{bmatrix} \mathbf{d}_1 \\ \mathbf{d}_2 \\ \vdots \\ \mathbf{d}_N \end{bmatrix} (N \equiv NP) \tag{3.33}$$

$$L_{IJ} = \Psi_I^X(\mathbf{X}_J) \tag{3.34}$$

where $\boldsymbol{\Lambda}$ is the coordinate transformation matrix and $\mathbf{I}$ is the identity matrix. The shape functions can also be transformed by

$$\hat{\Psi}_J(\mathbf{X}) = \sum_{I=1}^{\mathrm{NP}} L_{JI}^{-1} \Psi_I(\mathbf{X}) \tag{3.35}$$

and

$$u_i^h(\mathbf{X},t) = \sum_{I=1}^{\mathrm{NP}} \Psi_I^X(\mathbf{X}) d_{iI}(t) = \sum_{I=1}^{\mathrm{NP}} \hat{\Psi}_I^X(\mathbf{X}) \hat{d}_{iI}(t) \tag{3.36}$$

Note that $\hat{\Psi}_I(\mathbf{X}_J) = \delta_{IJ}$, and with this transformation, the essential boundary conditions of Eq. (3.31) are imposed by

$$\left.\begin{aligned} \hat{d}_{iI}(t) &= g_i(\mathbf{X}_I,t) \\ \delta \hat{d}_{iI}(t) &= 0 \end{aligned}\right\} \quad \forall I \in \eta_{g_i} \tag{3.37}$$

Using the Lagrangian reproducing kernel shape functions, the transformation matrix is formed only once and that can be performed at the undeformed configuration or even at a pre-processing stage.

The incremental matrix equation is obtained by introducing reproducing kernel shape function and coordinate transformation to the variational equation Eq. (3.4) and its linearization Eq. (3.7) to yield

$$\hat{\mathbf{M}} \Delta \ddot{\hat{d}} + \hat{\mathbf{K}} \Delta \hat{\mathbf{d}} = (\hat{\mathbf{f}}^{\mathrm{ext}})_{n+1} - (\hat{\mathbf{f}}^{\mathrm{int}})_{n+1}^{\nu} \tag{3.38}$$

where n and ν are the time step and iteration counters, respectively, $\Delta \mathbf{d} = \mathbf{d}_{n+1}^{\nu+1} - \mathbf{d}_{n+1}^{\nu}$ is the displacement increment, and $\hat{\mathbf{M}}$, $\hat{\mathbf{K}}$, $\hat{\mathbf{f}}^{\mathrm{ext}}$, and $\hat{\mathbf{f}}^{\mathrm{int}}$ are the mass matrix, stiffness

matrix, external force vector, and internal force vector at the nodal coordinates. Note that the matrices $\hat{\mathbf{M}}$, $\hat{\mathbf{K}}$, $\hat{\mathbf{f}}^{\text{ext}}$ and $\hat{\mathbf{f}}^{\text{int}}$ can be constructed directly by using the transformed Lagrangian reproducing kernel shape functions $\hat{\Psi}_I^{X/S}$, or by constructing their generalized coordinate counterparts using the untransformed Lagrangian reproducing kernel shape functions $\Psi_I^{X/S}$ and then performing matrix transformation to the nodal coordinates [see Chen et al. (1996) for details]. For example, $\hat{\mathbf{K}} = \mathbf{\Lambda}^{-1}\mathbf{K}\mathbf{\Lambda}^{-\mathrm{T}}$ where $\mathbf{K}$ is the stiffness formulated at the generated coordinates.

4 Frictional contact conditions

4.1 Preliminaries

In this development, we restrict the scope to the numerical treatment of contact conditions of a classical Coulomb friction law. For a general description of contact conditions, the two potential contact surfaces are arbitrarily designated by slave surface Γ_x^S and master surface Γ_x^M as shown in Fig. 3. At each point $x \in \Gamma_x^S$, a normal gap g_n is defined by

$$g_n = (\mathbf{x} - \mathbf{x}_C) \cdot \mathbf{n} \tag{4.1}$$

where $\mathbf{x}_C$ is the closest projection point of $\mathbf{x}$ onto Γ_x^M, i.e., $\|\mathbf{x} - \mathbf{x}_C\| = \min\{\|\mathbf{x} - \mathbf{x}^\star\| : \mathbf{x}^\star \in \Gamma_x^M\}$ and $\mathbf{n}$ is the unit outward normal vector of Γ_x^M at $\boldsymbol{x}_C$. The contact constraint does not allow the interpenetration to occur between Γ_x^S and Γ_x^M. When two surfaces Γ_x^S and Γ_x^M are in contact, the following constraint condition needs to be imposed

$$g_n = (\mathbf{x} - \mathbf{x}_C) \cdot \mathbf{n} = 0 \tag{4.2}$$

The friction between the contact surfaces are accounted for by the Coulomb law

$$\begin{cases} \text{if } | h_t | \leq \mu | h_n | \;\; g_t = 0 & \text{(stick)} \\ \text{otherwise} \;\; | h_t | = \mu | h_n | & \text{(slip)} \end{cases} \tag{4.3}$$

where h_t is the tangential traction with the direction opposite to the relative motion, μ is the coefficient of friction, and g_t is the tangential relative displacement increment during a load increment. The contact constraints are approximately furnished by a penalty formulation reduced from a perturbed Lagrange formulation (Saleeb et al. (1994)):

$$\delta\Pi(\mathbf{u}) + \int_{\Gamma_x^C} (\lambda_n \delta g_n + \lambda_t \delta g_t) \mathrm{d}\Gamma = 0, \quad \Gamma_x^C = \Gamma_x^S \cap \Gamma_x^M \tag{4.4}$$

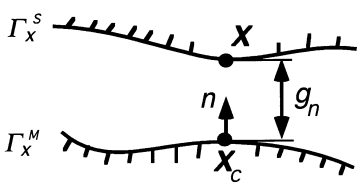

Fig. 3. Contact geometry and kinematics

where $\delta\Pi(\mathbf{u})$ is the virtual work without the contribution from the contact traction, and

$$\lambda_n = -\omega_n g_n \tag{4.5}$$

$$\lambda_t = \begin{cases} -\omega_t g_t & \text{if } | \omega_t g_t | \leq | \mu\lambda_n | \text{ (stick)} \\ -\mu\lambda_n \mathrm{sgn}(g_t) & \text{otherwise (slip)} \end{cases} \tag{4.6}$$

where ω_n and ω_t are the penalty numbers, and Eq. (4.6) is the penalized version of the classical Coulomb law.

4.2 Discretizations

To employ the slave-master slideline contact algorithm (Hallquist et al. (1985)), the master surface is represented by the union of master segments, and the slave surface is discretized by a set of slave nodes as shown in Fig. 4. In this work, we consider a piecewise linear discretization of the master segment. A typical situation is shown in Fig. 4, in which $\mathbf{x}_S = \mathbf{X}_S + \hat{\mathbf{d}}_S$ defines the current position of a slave node, and $\mathbf{x}_{M1} = \mathbf{X}_{M1} + \hat{\mathbf{d}}_{M1}$ and $\mathbf{x}_{M2} = \mathbf{X}_{M2} + \hat{\mathbf{d}}_{M2}$ define the current position of a master segment, where $\hat{\mathbf{d}}_S$, $\hat{\mathbf{d}}_{MI}$, $\hat{\mathbf{d}}_{M2}$ are the RKPM nodal displacements of the slave node S and master nodes $M1$ and $M2$. Note that in the search of contact conditions, the nodal kinematic information is required and therefore the nodal displacements are used here to define the kinematics for contact analysis. To define the contact geometry, the length l, the tangential unit vector $\mathbf{t}$, and the normal unit vector $\mathbf{n}$ of the linear master segment are defined as

$$l = \|\mathbf{x}_{M2} - \mathbf{x}_{M1}\|, \quad \mathbf{t} = \tfrac{1}{l}(\mathbf{x}_{M2} - \mathbf{x}_{M1}), \quad \mathbf{n} = \mathbf{e}_3 \times \mathbf{t} \tag{4.7}$$

where $\mathbf{e}_3$ is the base vector normal and pointing outward of the plane. The natural coordinate of a closest projection point $\mathbf{x}_C$ of $\mathbf{x}_S$ on the master segment $M1 - M2$ is described by the natural coordinate

$$\alpha_C = (\mathbf{x}_S - \mathbf{x}_{M1}) \cdot \mathbf{t}/l \tag{4.8}$$

and the location of $\boldsymbol{x}_C$ on the master segment is

$$\mathbf{x}_C = (1 - \alpha_C)\mathbf{x}_{M1} + \alpha_C \mathbf{x}_{M2} \tag{4.9}$$

The normal and tangential gaps associated with the slave nodes S and master segment $M1 - M2$ are defined as

$$g_n = (\mathbf{x}_S - \mathbf{x}_{M1}) \cdot \mathbf{n} \tag{4.10}$$

$$g_t = (\mathbf{x}_C - \mathbf{x}_C^0) \cdot \mathbf{t} \tag{4.11}$$

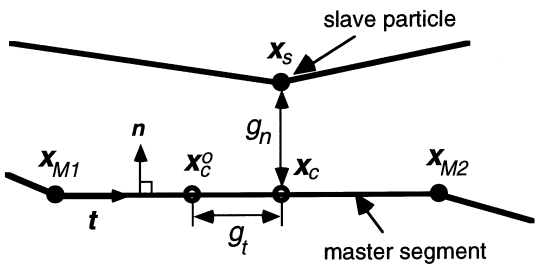

Fig. 4. Discretization of contact surfaces

where $\mathbf{x}_C^0 = (1-\alpha_C^0)\mathbf{x}_{M1} + \alpha_C^0\mathbf{x}_{M2}$ is the closest projection point of the slave node at the last converged increment and α_C^0 is its corresponding natural coordinate computed by Eq. (4.8). Note that in Eq. (4.11), the master segment refers to the last converged stage. The collocation discretization of Eq. (4.4) leads to

$$\delta U(\mathbf{u}) + \sum_A (\lambda_n \delta g_n + \lambda_t \delta g_t)_A = 0 \tag{4.12}$$

where A is summed over all the closest projection points of the slave nodes on the master segments, and $(\lambda_n \delta g_n + \lambda_t \delta g_t)_A$ denotes the evaluation of $\lambda_n \delta g_n + \lambda_t \delta g_t$ at the closest projection point x_A. Using the property $\hat{\Psi}_I^X(X_A) = \delta_{IA}$, the reproducing kernel particle discretization of the term $(\lambda_n \delta g_n + \lambda_t \delta g_t)_A$ is

$$(\lambda_n \delta g_n + \lambda_t \delta g_t)_A = \delta \hat{\mathbf{d}}_A^{\mathrm{T}} (\hat{\mathbf{f}}^C)_A \tag{4.13}$$

where $\hat{\mathbf{d}}_A$ is the composite *nodal* displacement vectors associated with the slave particle $\mathbf{x}_S$ and the two end points of the master segment $\mathbf{x}_{M1}$ and $\mathbf{x}_{M2}$,

$$\hat{\mathbf{d}}_A^{\mathrm{T}} = \left[\hat{\mathbf{d}}_S^{\mathrm{T}}, \hat{\mathbf{d}}_{M1}^{\mathrm{T}}, \hat{\mathbf{d}}_{M2}^{\mathrm{T}}\right] \tag{4.14}$$

and the corresponding *nodal* contact force vector at the closest projection point x_A is

$$(\hat{\mathbf{f}}^C)_A = (\lambda_n \mathbf{C}_n + \frac{l^0}{l}\lambda_t \mathbf{C}_t)_A \tag{4.15}$$

where

$$\mathbf{C}_n^{\mathrm{T}} = \left[\mathbf{n}^{\mathrm{T}}, -(1-\alpha_C)\mathbf{n}^{\mathrm{T}}, -\alpha_C \mathbf{n}^{\mathrm{T}}\right] \tag{4.16}$$

$$\mathbf{C}_t^{\mathrm{T}} = \left[\mathbf{t}^{\mathrm{T}}, \frac{-g_n}{l}\mathbf{n}^{\mathrm{T}} - (1-\alpha_C)\mathbf{t}^{\mathrm{T}}, -\frac{g_n}{l}\mathbf{n}^{\mathrm{T}} - \alpha_C \mathbf{t}^{\mathrm{T}}\right] \tag{4.17}$$

and $\mathbf{x}_A$ is the projection of $\mathbf{x}_S$ onto the $M1 - M2$ line. With the use of the transformation method, the RKPM contact force vector $\hat{\mathbf{f}}^C$ in Eq. (4.15) does not involve the reproducing kernel shape functions.

Taking the collocation form of $\Delta \int_{\Gamma_c} (\lambda_n \delta g_n + \lambda_t \delta g_t) \mathrm{d}\Gamma$ in conjunction with the Kronecker delta property of transformed Lagrangian reproducing kernel shape functions $\{\hat{\Psi}_I^X\}_{I=1}^{\mathrm{NP}}$ yields the following RKPM discretized tangential operator associated with the contact constraints:

$$[\Delta(\lambda_n \delta g_n + \lambda_t \delta g_t)]_A = \delta \hat{\mathbf{d}}_A^{\mathrm{T}} (\hat{\mathbf{K}}^C)_A \Delta \hat{\mathbf{d}}_A \tag{4.18}$$

where $(\mathbf{K}^C)_A$ is the contact stiffness matrix with the component ordering consistent with $[\hat{\mathbf{d}}]_A$:

$$(\hat{\mathbf{K}}^C)_A = \left\{ \omega_n \mathbf{C}_n \mathbf{C}_n^{\mathrm{T}} + \frac{\lambda_n}{l}(\mathbf{P}\mathbf{T}^{\mathrm{T}} + \mathbf{T}\mathbf{P}^{\mathrm{T}} + \frac{g_n}{l}\mathbf{P}\mathbf{P}^{\mathrm{T}}) - \frac{\lambda_t l^0}{l^2}\left[C_n \mathbf{P}^{\mathrm{T}} + \mathbf{P}\mathbf{C}_n^{\mathrm{T}} - \frac{g_n}{l}(\mathbf{P}\mathbf{Q}^{\mathrm{T}} + \mathbf{Q}\mathbf{P}^{\mathrm{T}}) - C_t Q^{\mathrm{T}} - Q C_t^{\mathrm{T}} \right] \right\}_A + (\hat{\mathbf{K}}^f)_A \tag{4.19}$$

and

$$(\hat{\mathbf{K}}^f)_A = \begin{cases} \frac{l^0}{l}\omega_t (\mathbf{C}_t \mathbf{C}_t^{\mathrm{T}})_A & \text{if } |\omega_t g_t| \leq |\mu \lambda_n| \\ -\frac{l^0}{l}\mu\omega_n [\mathrm{sgn}(g_t)\mathbf{C}_t \mathbf{C}_n^T]_A & \text{otherwise} \end{cases} \tag{4.20}$$

$$\mathbf{P}^{\mathrm{T}} = \left[\mathbf{0}^{\mathrm{T}}, -\mathbf{n}^{\mathrm{T}}, \mathbf{n}^{\mathrm{T}}\right] \tag{4.21}$$

$$\mathbf{Q}^{\mathrm{T}} = [\mathbf{0}^{\mathrm{T}}, -\mathbf{t}^{\mathrm{T}}, \mathbf{t}^{\mathrm{T}}] \tag{4.22}$$

$$\mathbf{T}^{\mathrm{T}} = [\mathbf{t}^{\mathrm{T}}, -(1-\alpha_C)\mathbf{t}^{\mathrm{T}}, -\alpha_C \mathbf{t}^{\mathrm{T}}] \tag{4.23}$$

Combining Eqs. (3.38), (4.13), and (4.18), the final incremental reproducing kernel matrix equation of a contact problem is

$$\hat{\mathbf{M}}\Delta\ddot{\hat{\mathbf{d}}} + (\hat{\mathbf{K}} + \hat{\mathbf{K}}^C)_{n+1}^{\nu} \Delta \hat{\mathbf{d}} = (\hat{\mathbf{f}}^{\mathrm{ext}})_{n+1} - (\hat{\mathbf{f}}^{\mathrm{int}} + \hat{\mathbf{f}}^C)_{n+1}^{\nu} \tag{4.24}$$

where $\hat{\mathbf{K}}$ and $\hat{\mathbf{f}}^{\mathrm{int}}$ are global tangential stiffness matrix and internal force vector associated with the non-contact conditions.

4.3 Degeneration to quasi-static rigid-to-flexible body frictional contact

Many metal forming processes are slow in motion, and the problems can be treated as quasi-static in which the inner effect is neglected:

$$(\hat{\mathbf{K}} + \hat{\mathbf{K}}^C)_{n+1}^{\nu} \Delta \hat{\mathbf{d}} = (\hat{\mathbf{f}}^{\mathrm{ext}})_{n+1} - (\hat{\mathbf{f}}^{\mathrm{int}} + \hat{\mathbf{f}}^C)_{n+1}^{\nu} \tag{4.25}$$

If one further assumes that the master surfaces are rigid (for example, punch and die) with prescribed rigid body motion, then the degrees of freedom associated with the master segments can be eliminated from the system of algebraic equations. In this case, the composite contact nodal displacement vector of Eq. (4.14) reduces to

$$\hat{\mathbf{d}}_A^{\mathrm{T}} = \hat{\mathbf{d}}_S^{\mathrm{T}} \tag{4.26}$$

and the corresponding *nodal* contact force vector at the closest projection point x_A is

$$(\hat{\mathbf{f}}^C)_A = (\lambda_n \mathbf{n}^{\mathrm{T}} + \lambda_t \mathbf{t}^{\mathrm{T}})_A \tag{4.27}$$

Consequently, the contact stiffness matrix $(\mathbf{K}^C)_A$ corresponding to $\hat{\mathbf{d}}_A$ reduces to:

$$(\hat{\mathbf{K}}^C)_A = (\omega_n \mathbf{n}\mathbf{n}^{\mathrm{T}})_A + (\hat{\mathbf{K}}^f)_A \tag{4.28}$$

and

$$(\hat{\mathbf{K}}^f)_A = \begin{cases} \omega_t (\mathbf{t}\mathbf{t}^{\mathrm{T}})_A & \text{if } |\omega_t g_t| \leq |\mu \lambda_n| \\ -\mu\omega_n [\mathrm{sgn}(g_t)\mathbf{t}\mathbf{n}^{\mathrm{T}}]_A & \text{otherwise} \end{cases} \tag{4.29}$$

5 Numerical examples

Lagrangian reproducing kernel shape functions constructed by the cubic B-splice kernel function with linear basis functions $\mathbf{H}^{\mathrm{T}} = [1, X - X_I, Y - Y_I]$ are used to analyze the numerical examples. In the following problems, the metal forming processes are considered to be quasi-static, and punch and die are assumed to be perfectly rigid.

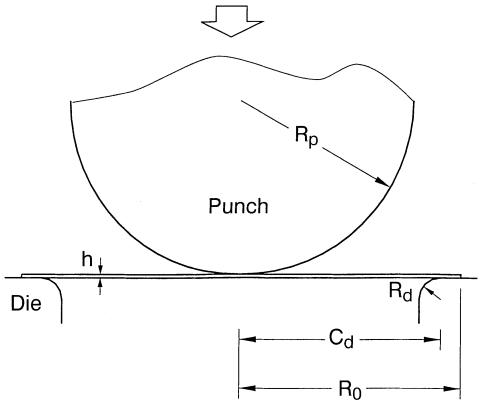

Fig. 5. Geometric description of cylindrical punch stretch

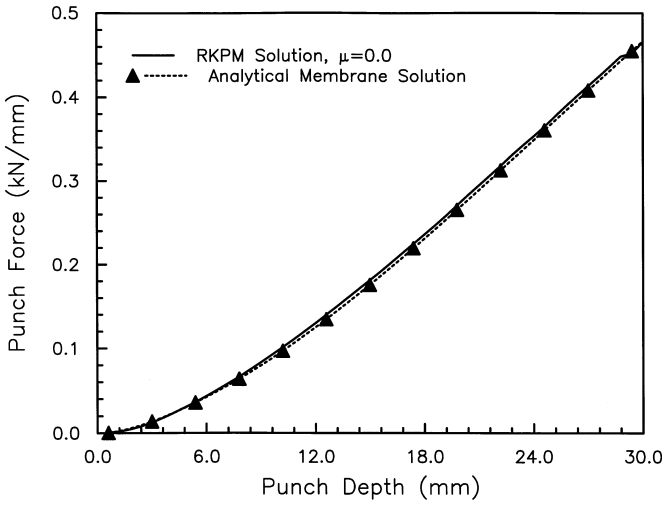

Fig. 6. Cylindrical punch stretch: comparison with membrane solution

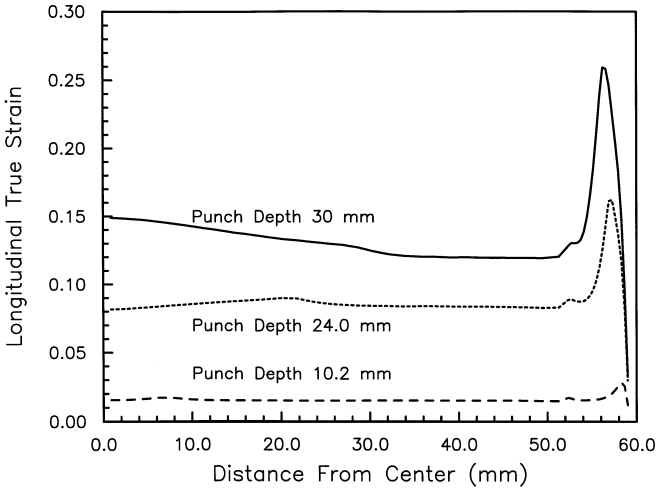

Fig. 7. Cylindrical punch stretch: longitudinal true strain distribution

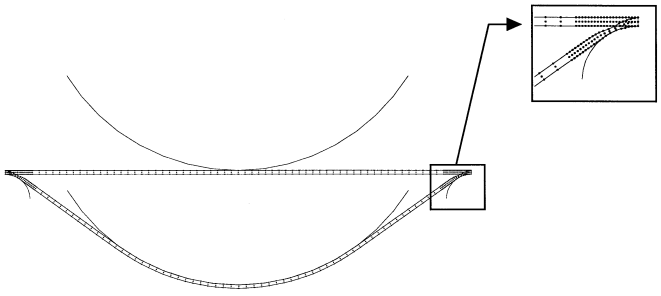

Fig. 8. Cylindrical punch stretch: deformation at punch depth of 30 mm

5.1
Sheet metal stretch by a cylindrical punch

This problem is advocated as a benchmark test [Choudhry and Lee (1994)] of sheet metal forming processes. A plane-strain sheet metal is stretched by a cylindrical punch as shown in Fig. 5, where the geometrical parameters are $R_p = 50.8$ mm, $C_d = 59.18$ mm, $R_d = 6.35$ mm, and $h = 1$ mm. The material constants of the sheet metal are as follows: Young's modulus $E = 69$ GPa, Poisson's ratio $v = 0.3$, isotropic hardening $R(\bar{\varepsilon}^p) = 589(10^{-4} + \bar{\varepsilon}^p)^{0.216}$ MPa, and coefficient of friction $\mu = 0$. Because of symmetry, only half of the sheet metal is modeled with 3×51 particles and 2×50 integration zones, and Gauss integration order of 4×4 is used. Normalized dilation parameter (dilation parameter "a" in Eq. (3.12) divided by the nodal distance) of 1.4 is employed in both membrane and thickness directions. Relative dense particles are distributed around the die where the sharp corner is expected to cause stress concentrations. In this analysis, the end of the sheet metal is fixed, and the rigid punch is moved downward with a vertical displacement of 30 mm in 50 incremental steps.

The RKPM prediction is compared with the membrane analytical solution [Choudhry and Lee (1994)] and good agreement is observed in Fig. 6. Figure 7 shows the excessive deformation that occurs near the contact with the die at various deformation stages. The final deformation of the sheet metal is shown in Fig. 8, and local neckings are observed near the die contact areas. In this analysis, the tolerance for the residual force norm is 10^{-6}. A typical residual force norm information during the iteration process at the punch depth of 27 mm is shown in Tables 1, and a quadratic convergent rate is observed. An average of 12 iterations is required in each incremental step. In this analysis, the RKPM solution is not sensitive to the dilatational parameters.

5.2
Sheet metal stretch by a hemispherical punch

This problem is the axisymmetric version of the preceding one, and the same analysis model and conditions are used. In this problem, frictionless ($\mu = 0$) and frictional ($\mu = 0.3$) conditions are considered, and the predicted punch force-displacement curves are plotted in Fig. 9. Stiffer response of the frictional case occurs only at a deeper punch depth. The longitudinal true strain distributions are shown in Figs. 10 and 11, and the friction shifts the strain peak away from the center line.

Table 1. Sheet metal stretch by cylindrical punch: force residual norms at punch depth 27 mm

Iteration	1	2	3	4	5	6
force residual norm	.12087E+04	.94854E+03	.25455E+03	.14846E+03	.99999E+02	.44881E+02
	7	8	9	10	11	12
	.12087E+04	.94854E+03	.25455E+03	.14846E+03	.99999E+02	.44881E+02
	13	14	15	16	17	18
	.16754E+02	.16823R+02	.12630E+01	.12677E-01	.20761E-05	.31347E-09

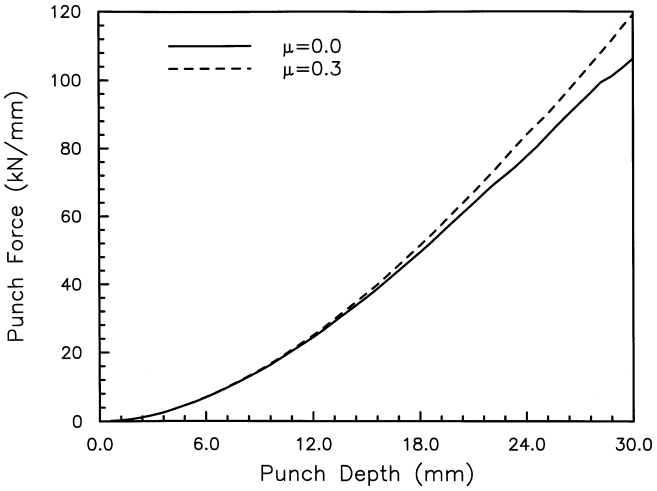

Fig. 9. Hemispherical punch stretch: load-displacement curves of $\mu = 0.0$ and 0.3

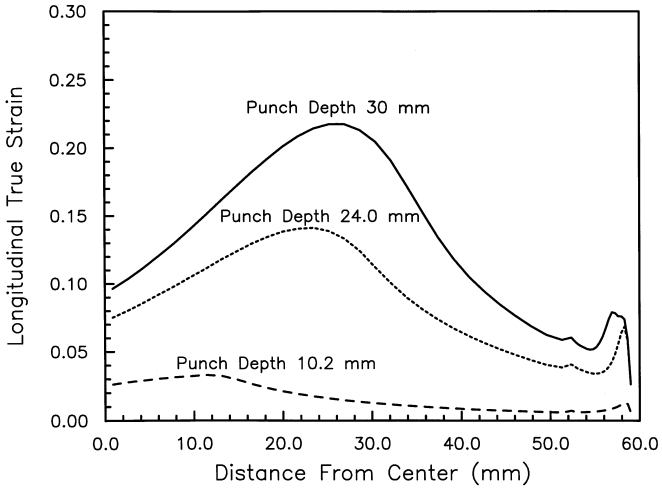

Fig. 11. Hemispherical punch stretch: longitudinal true strain distribution at various punch depth with $\mu = 0.3$

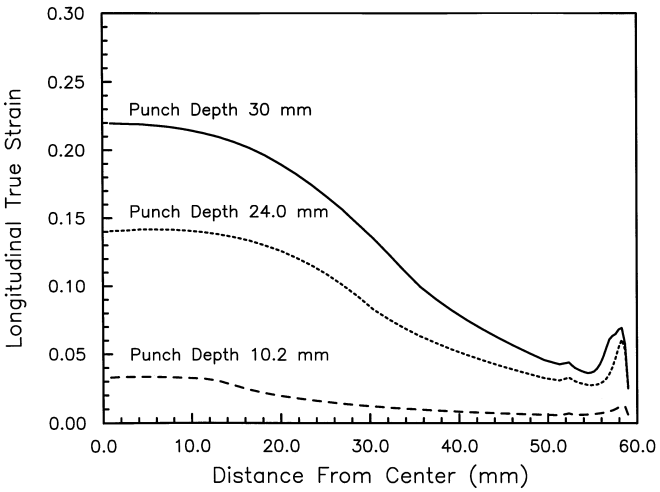

Fig. 10. Hemispherical punch stretch: longitudinal true strain distribution at various punch depth with $\mu = 0.0$

In this analysis the tolerance of the residual force norm is chosen to be 10^{-6}, and an average of 9 iterations is required for both frictionless and frictional cases. A typical residual force norm information at punch depth of 27 mm is shown in Table 2, and the quadratic convergent rates are observed.

Table 2. Sheet metal stretch by a hemispherical punch: force residual norms at punch depth 27 mm

Iteration	Force residual norm ($\mu = 0$)	Force residual norm ($\mu = 0.3$)
1	.29995E+05	.34642E+05
2	.16242E+05	.17483E+05
3	.27556E+04	.21240E+04
4	.11993E+04	.27415E+04
5	.47132E+02	.55116E+02
6	.83472E+00	.19323E+01
7	.53776E−03	.64199E−02
8	.62826E−07	.15286E−06

5.3 Ring compression analysis

The ring compression test is often used to estimate the friction coefficient in metal forming operations [Male and Cockcroft (1965)]. The test consists of compressing a ring at different compression ratios with flat tools and measuring the deformed height and deformed internal diameter. The setup of the ring test is shown in Fig. 12, where the initial ring geometry is: internal diameter = 6.0 cm, height = 4.0 cm, and external diameter = 12.0 cm. The ring is made of a cold forging steel 16MnCr5 with yield stress $\sigma_y = 100$ MPa, Young's modulus $E = 288$ GPa, Poisson's ratio $\nu = 0.3$, and the material is assumed to be perfectly plastic.

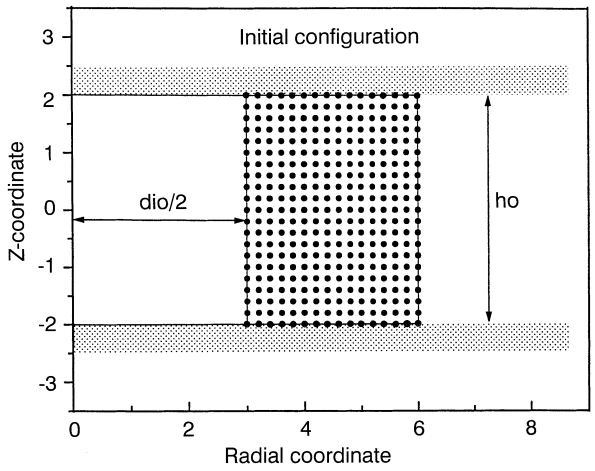

Fig. 12. Geometric description of ring compression

Due to symmetry, only a quarter of the ring is discretized by 16×11 nodes and 15×10 integration zones as shown in Fig. 12. The dilation parameters ("a" in Eq. (3.21)) is 0.6 cm in x- and y-directions and the Gauss integration order is 4×4. Several analyses were performed with various friction conditions $\mu = 0.0, 0.15, 0.3$, and with perfect stick conditions. The ring is compressed to half of its original height in 1000 incremental steps. Due to the frictional contact conditions, bulge deformation occurs, and the degree of bulging is proportional to the level of friction on the interface. The final deformations of the RKPM analysis for different frictional conditions are shown in Fig. 13, and as expected the bulge deformation is most severe in the stick condition. Figure 14 shows the ring progressive deformations of the stick condition, and the effective plastic strain contour is plotted in Fig. 15.

A refined model with h-adaptivity at the four corners is introduced to better capture the strain concentration under stick condition. The original and deformed geometries of the refined model subjected to stick condition are plotted in Fig. 16, and the corresponding effective plastic strain is shown in Fig. 17.

Finite element analysis is also performed for the stick condition using ABAQUS. Automatic time stepping is used with an initial step size set to be 0.1% of the total compression, and with the maximum increment specified to be

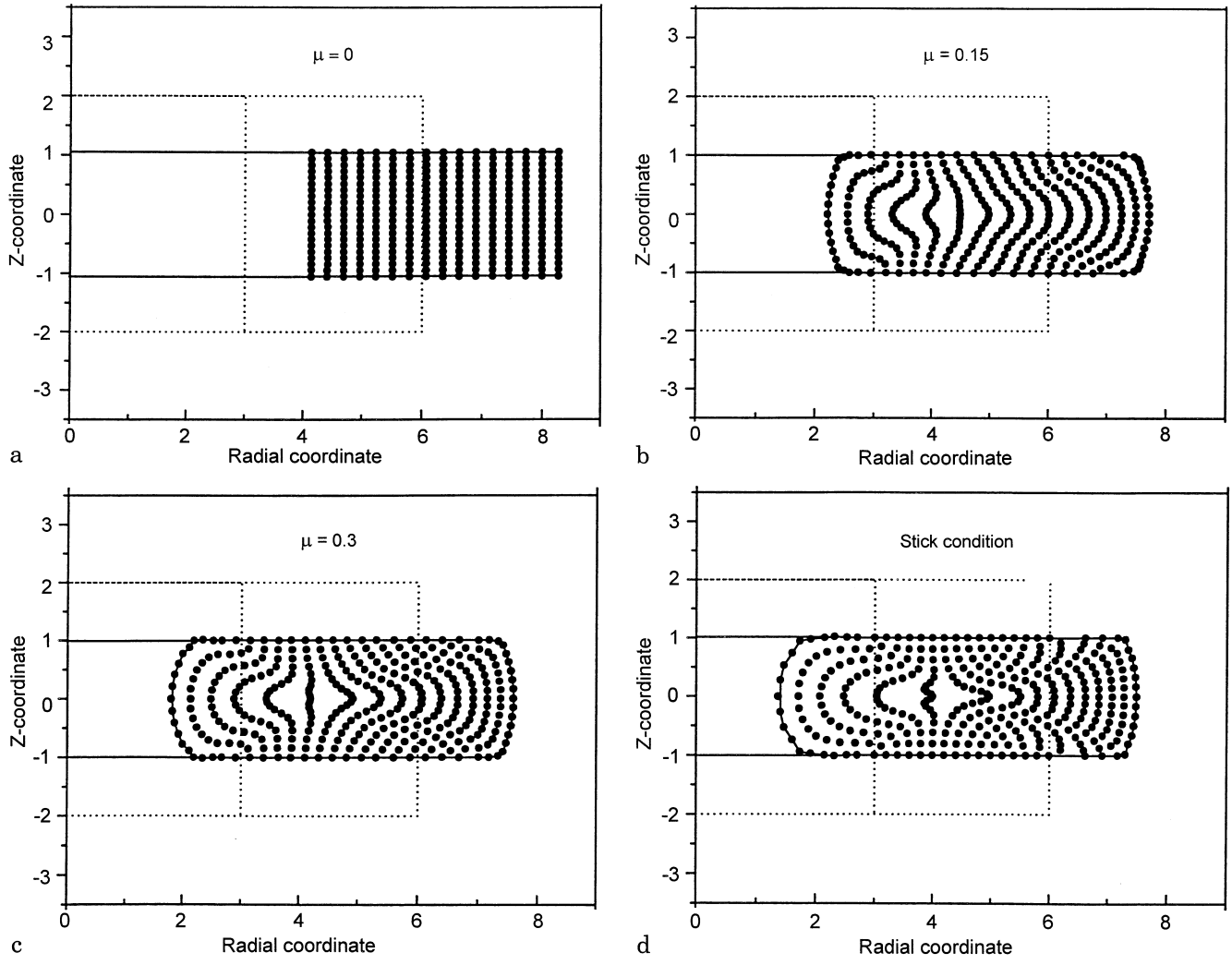

Fig. 13a–d. Ring compression: final deformed geometries associated with various frictional conditions: **a** $\mu = 0.0$, **b** $\mu = 0.15$, **c** $\mu = 0.3$, **d** stick

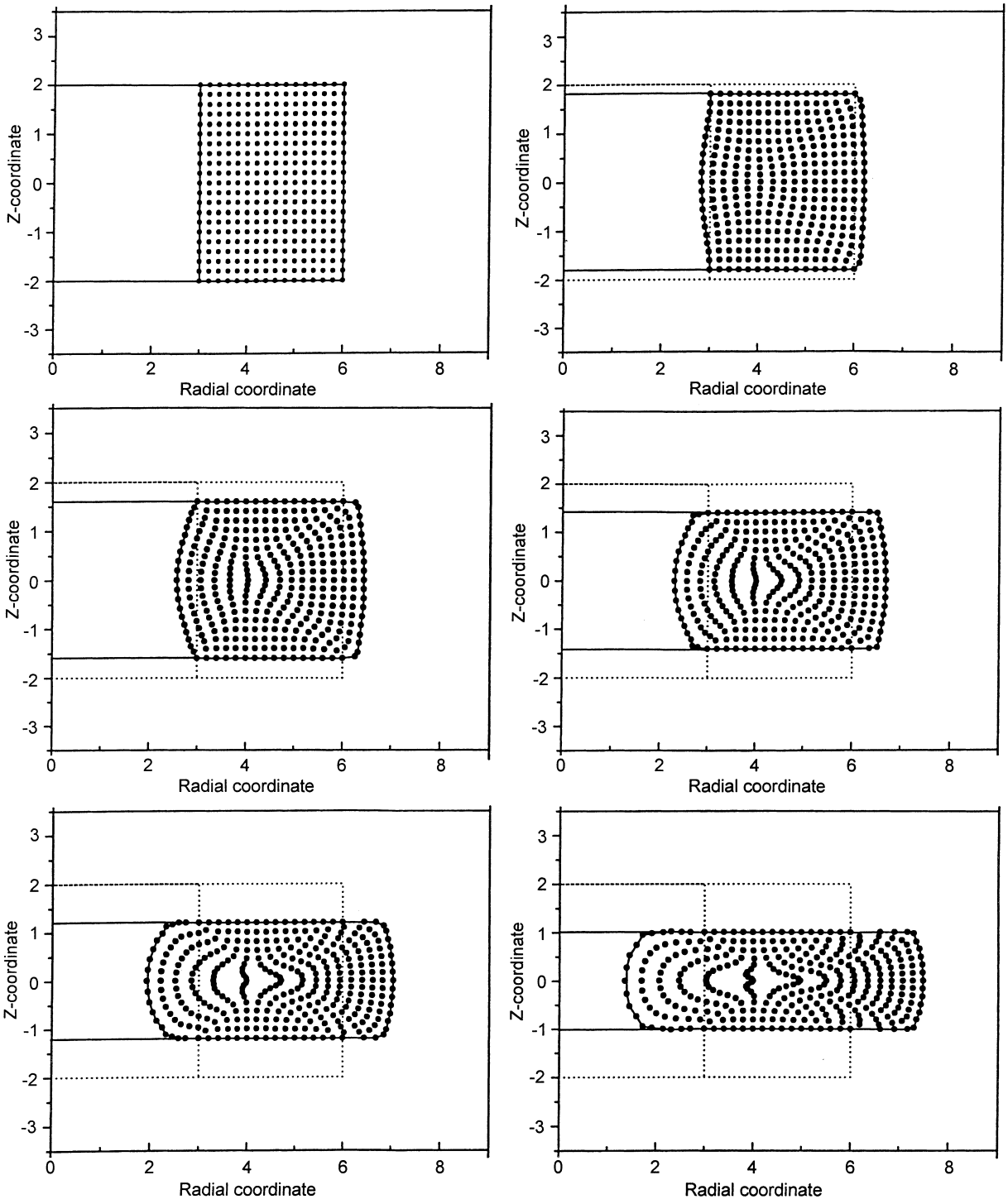

Fig. 14. Ring compression: progressive deformations associated with stick condition

1000. Both 4-node and 8-node elements with various formulations available in ABAQUS, including hybrid formulation and displacement-based formulation with reduced integration and hourglass control, are used to analyze this ring compression problem under stick condition. All the finite element analyses failed when dealing with the stick condition since it leads to a severe mesh distortion. Figure 18 shows the distorted meshes of 4-node and 8-node hybrid elements prior to the solution divergence.

5.4 Upsetting simulation

An upsetting process with the axisymmetric geometries of the punch, die, workpiece, and their initial setup as shown in Fig. 19 is analyzed using RKPM. The punch and die are treated as rigid bodies, and only the workpiece is considered to be deformable. The material properties of the workpiece are: Young's modulus $E = 288$ GPa, Poisson's ratio $\nu = 0.3$, and the material is assumed to be perfectly

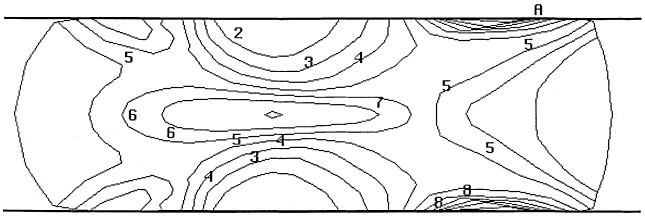

Fig. 15. Ring compression: effective plastic strain distribution of stick condition

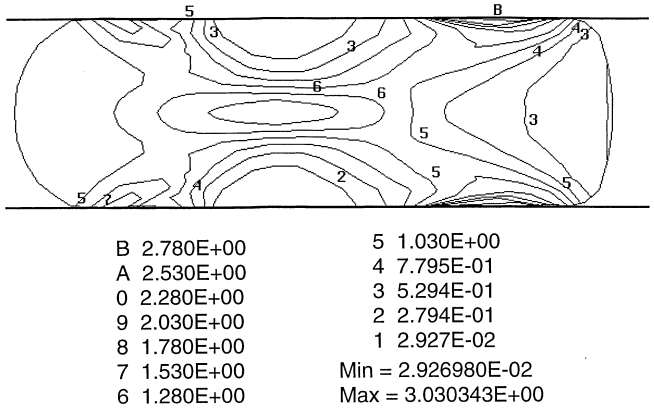

Fig. 17. Ring compression: effective plastic strain of corner-refined model under stick condition

plastic with the yield stress $\sigma_y = 100$ MPa. The friction between the punch/die and the workpiece was determined based on lubrication conditions. In this problem the coefficient of friction is estimated to be $\mu = 0.15$ [Roque (1996)]. During the upsetting operation, the die is totally fixed, and the punch is compressed until the punch/die is completely closed.

The workpiece model is created by MSC/PATRAN as shown in Fig. 20, in which the finite element mesh is used as the integration zones for RKPM computation. The supports of the kernel function (Eq. (3.12)) cover about five particles in each direction. All the particles on the surface of the workpiece, except the ones on the line of symmetry, are assigned as the slave particles since they all have the possibility to contact with the punch or die. The master segments on the die are completely fixed, and the master segments of the punch are moved downward with a total travel of 1.68 cm to close the opening. The progressive deformations of the workpiece are shown in Fig. 21. The comparison of the predicted deformation and the experimental data [Roque (1996)] as

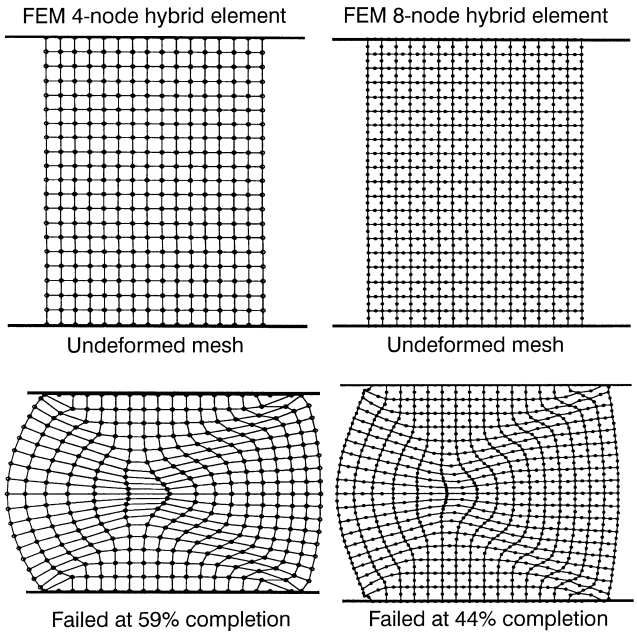

Fig. 18. Finite element analysis of ring compression problem

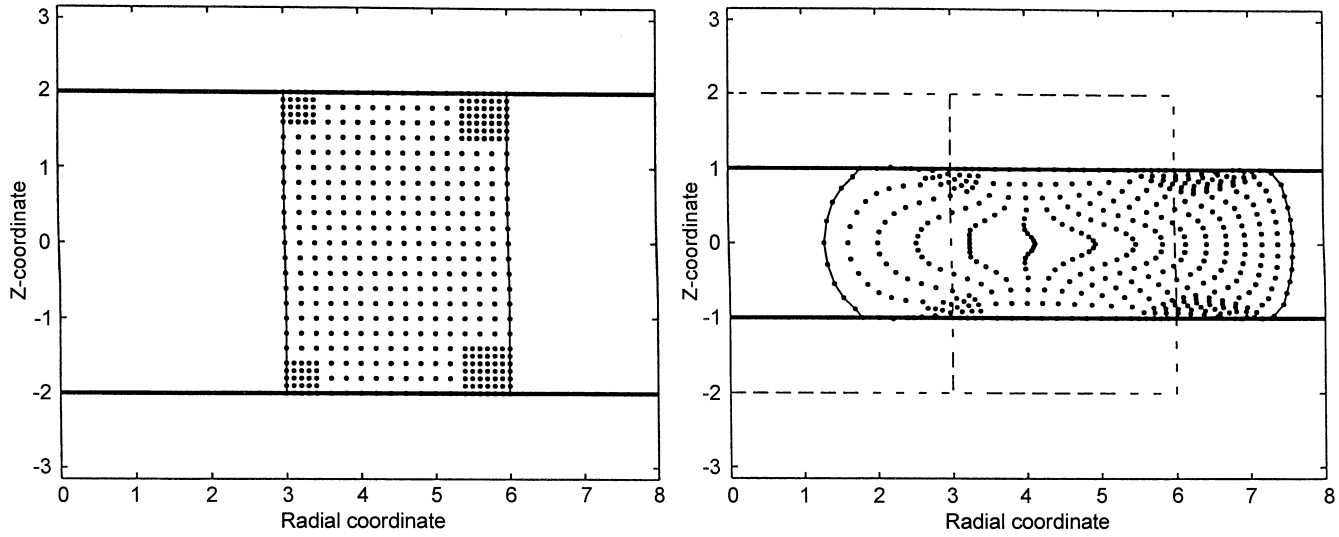

Fig. 16. Ring compression: final deformation of corner-refined model under stick condition

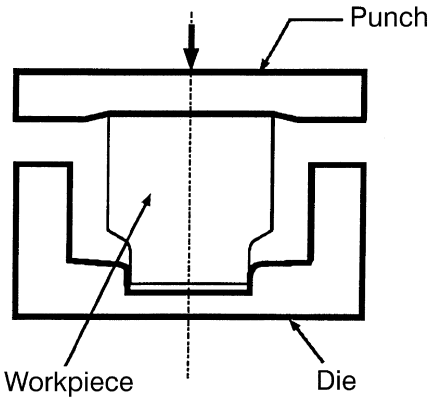

Fig. 19. Geometric description of an upsetting process

given in Fig. 22 demonstrates a satisfactory performance of RKPM.

6 Conclusions

In this paper, a meshless formulation for loading path-dependent material behavior and frictional contact conditions is developed based on the Reproducing Kernel

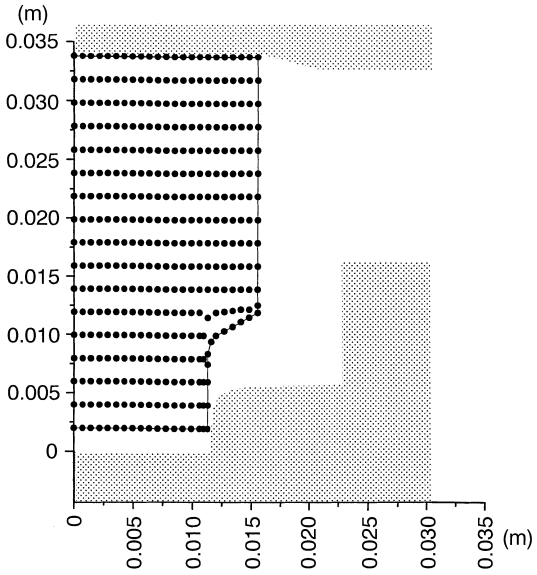

Fig. 20. Upsetting process: RKPM analysis model and contact surfaces

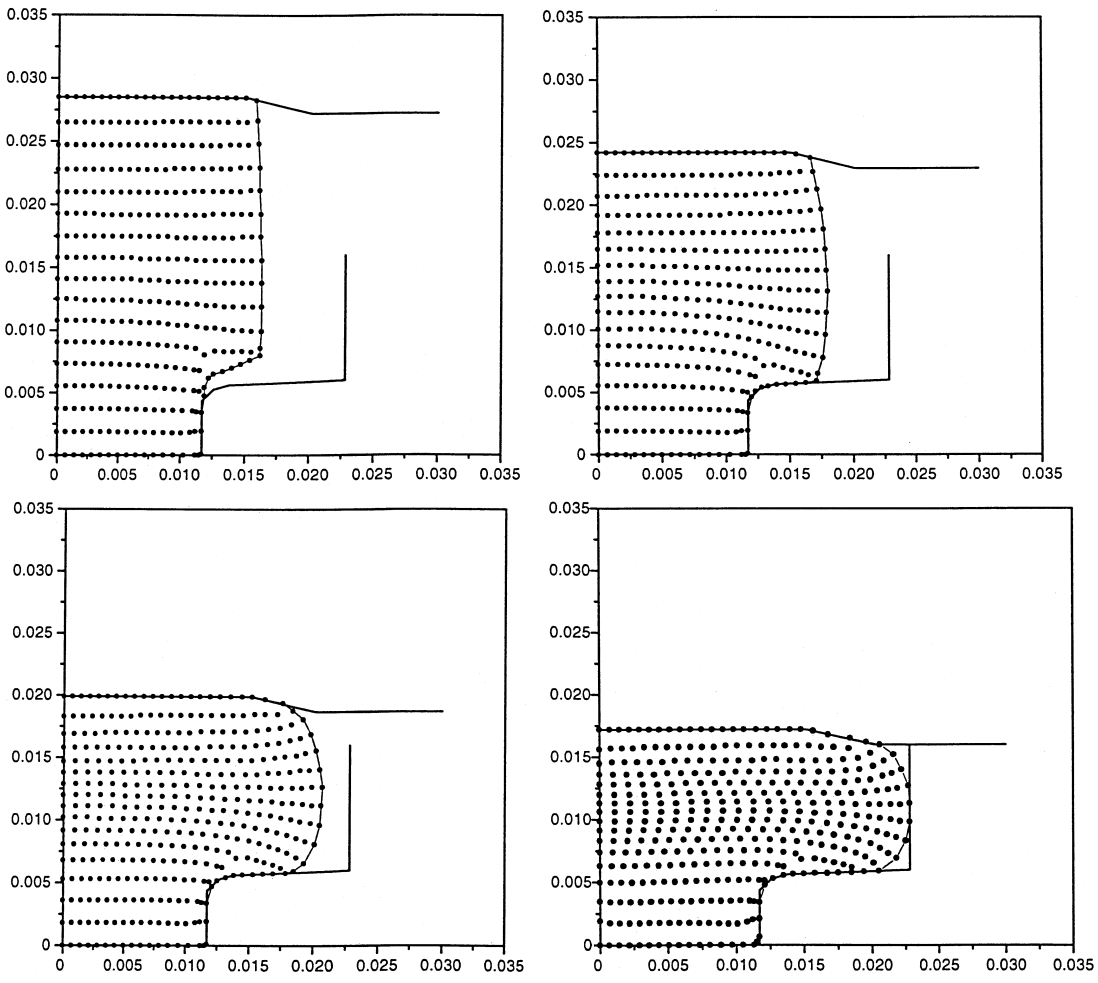

Fig. 21. Upsetting process: progressive deformations

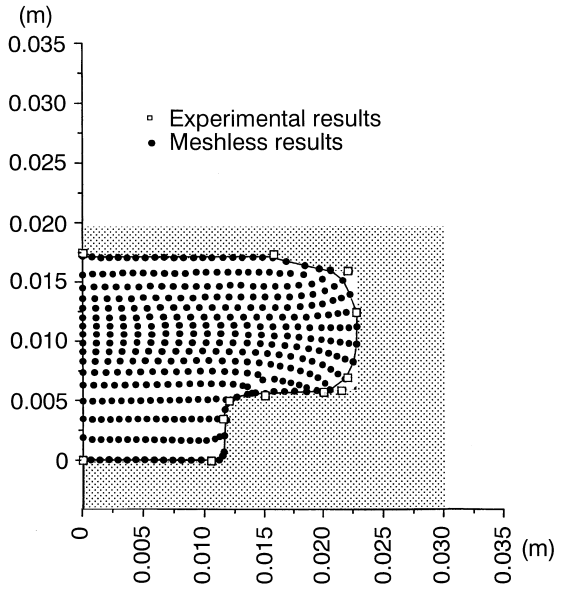

Fig. 22. Upsetting process: RKPM comparison with experimental measurement

Particle Method (RKPM). Both Lagrangian (material) and Eulerian (spatial) forms of the reproducing kernel shape functions can be used to approximate the field variables of path-dependent materials. The employment of Lagrangian reproducing kernel shape functions leads to a straightforward computation of the material time derivative of displacements; however, performing the spatial derivative of displacements requires the inversion of the deformation gradient. Conversely, using the Eulerian reproducing kernel shape functions allows direct computation of the spatial derivatives of displacements, but it yields an additional convective term when performing material time derivative of displacements.

In this work, the Lagrangian reproducing kernel shape functions are constructed for the discretization of the variational equation expressed in the current configuration. The generalized displacements are transformed to the nodal coordinates to yield a direct treatment of essential boundary conditions and concentrated loads. With the employment of the Lagrangian reproducing kernel shape functions, the transformation matrix, and its inversion, can be computed at a pre-processing stage. The RKPM computation requires that the support of the kernel function covers enough particles, and the use of Lagrangian reproducing kernel shape functions assures this kernel stability in large deformation analysis since they cover the same set of particles throughout the deformation processes.

This coordinate transformation method also leads to a straightforward implementation of contact formulation and contact algorithms in a meshless setting. To maintain the consistency between the treatment of contact constraints and essential boundary conditions, a collocation discretization is employed to construct a nodal contact force vector and a contact stiffness matrix. Since in this formulation all the kinematic quantities are computed at the nodes, using the transformed reproducing kernel shape functions yields simple expressions in the RKPM matrix equation for contact problems.

The numerical examples demonstrate the effectiveness of Lagrangian RKPM for metal forming analysis. The large plastic deformation induced in the metal forming process can be dealt with easily by the proposed method, and no mesh distortion difficulties are encountered. Due to the use of the Lagrangian reproducing kernel shape functions, the support size of the kernel functions does not require re-adjustment during the contact computation.

References

Atluri SN (1980) On some new general and complementary energy theorems for the rate problems in finite strain, classical elastoplasticity. J. Struct. Mech. 8 (1):61–92

Atluri SN (1984) On constitutive relations at finite strain: hypo-elasticity and elasto-plasticity with isotropic or kinematic hardening. Comput. Meth. Appl. Mech. Eng. 43:137–171

Atluri SN, Cazzani A (1995) Rotations in computational solid mechanics. Invited feature article, Arch. Comput. Meth. Eng. ICNME, Barcelona, Spain, 2 (1):49–138

Babuska I (1973) The finite element method with Lagrangian multipliers. Numer. Math. 20:179–192

Brezzi F (1974) On the existence, uniqueness and approximation of saddle-point problems arising from Lagrange multipliers. RAIRO Anal. Numer. 8:129–151

Babuska I, Melenk JM (1997) The partition of unity method. in press, Int. J. Numer. Meth. Eng, 40: 727–758

Belytschko T, Kennedy JM (1978) Computer methods for subassembly simulation. Nucl. Eng. Des. 49:17–38

Belytschko T, Gu L, Lu YY (1994) Fracture and crack growth by EFG method. Model. Simul. Mater. Sci. Eng. 2:519–534

Belytschko T, Organ D, Kronggauz Y (1995) A coupled finite element-element-free galerkin method. Comput. Mech. 17:186–195

Belytschko T, Tabbara M (1996a) Dynamic fracture using element-free galerkin methods. Int. J. Numer. Meth. Eng. 39:923–938

Belytschko T, Kronggauz Y, Organ D, Fleming M (1996b) Meshless methods: an overview and recent developments. Comput. Meth. Appl. Mech. Eng. 139:3–47

Benson DJ (1989) An efficient, accurate, simple ALE method for nonlinear finite element programs, Comput. Meth. Appl. Mech. Eng. 72:305–350

Chen JS, Pan C, Wu CT, Liu WK (1996) Reproducing kernel particle methods for large deformation analysis of nonlinear structures, Comput. Meth. Appl. Mech. Eng. 139:195–229

Chen JS, Pan C, Wu CT (1997a) Reproducing kernel particle methods for rubber hyperelasticity. Comput. Mech. 19:211–227

Chen JS, Yoon S, Liu WK (1997b) An improved reproducing kernel particle method for nearly incompressible hyperelastic solids. submitted, Comput. Meth. Appl. Mech. Eng

Chen JS, Chang KH, Hardee E, Yoon S, Kaneko M, Grindeanu I (1997c) A structural nonlinear analysis workspace (SNAW) based on meshless methods. in press, Advances in Engineering Software

Chen JS, Pan C, Wu CT (1998) Applications of reproduction kernel particle method to large deformation and contact analysis of elastomers. Rubber Chemistry and technology, 71:191–213

Choudhry S, Lee JK (1994) Dynamic plane-strain element simulation of industrial sheet-metal forming processes. Int. J. Mech. Sci. 36:189–207

Dawson PR (1978) Viscoplastic finite element analysis of steady state forming processes including strain history and stress flux dependence. Appl. Numer. Meth. Form. Proc. ADM Vol. 28, ASME, New York, pp 55–66
Donea J, Fasoli-Stella P, Guiliani S (1977) Lagrangian and eulerian finite element techniques for transient fluid-structure interaction problems. Trans. 4th SMIRT Conf., San Francisco, Paper B1/2
Duarte CA (1995) An review of some meshless methods to solve partial differential equations. Tech. Report 95-06, TICAM, The University of Texas at Austin
Duarte CA, Oden JT (1996) An h-p adaptive method using clouds. Comput. Meth. Appl. Mech. Eng. 139:237–262
Ghosh S, Kikuchi N (1988) Finite element formulation for the simulation of hot sheet metal forming processes. Int. J. Eng. Sci. 26:143–161
Grindeanu I, Chang KH, Choi KK, Chen JS (1996) Shape design sensitivity analysis of hyperelastic structures using a meshless method. accepted, AIAA Journal
Grindeanu I, Chang KH, Choi KK, Chen JS (1997) Design sensitivity analysis and optimization for hyperelastic materials using meshless methods. to submit, AIAA Journal
Günther FC, Liu WK (1997) Implementation of boundary conditions for meshless methods. submitted, Comp. Meth. Appl. Mech. Eng
Haber RB, Hariandia RH (1985) An Eulerian-Lagrangian finite element approach to large-deformation frictional contact. Comp. Struct. 20:193–201
Hallquist JO, Goudreau GJ, Benson DJ (1985) Sliding interfaces with contact-impact in large scale Lagrangian computations. Comp. Meth. Appl. Mech. Eng. 51:107–137
Hu Y.-K, Liu WK (1993) An ALE hydrodynamic lubrication finite element method with application to strip rolling. Int. J. Numer. Meth. Fluids 36:855–880
Hughes TJR, Winget JM (1980) Finite rotation effects in numerical integration of rate constitutive equations arising in large deformation analysis. Int. J. Numer. Meth. Eng. 16:1862–1867
Hwu Y.-J, Lenard JG (1988) A finite element study of flat rolling. J. Eng. Mater. Technol. ASME, 110:22–27
Keck P, Wilhelm M, Lange K (1990) Application of the finite element method to the simulation of metal forming processes comparison and calculations and experiments. Int. J. Mech. Eng. 30:1415–1430
Lancaster P, Salkauskas K (1981) Surfaces generated by moving least squares methods. Math. Comput. 37:141–158
Li S, Liu WK (1996) Moving least-square reproducing kernel method, Part II: Fourier analysis. Comput. Meth. Appl. Mech. Eng. 139:159–193
Li S, Liu WK (1997a) Synchronized reproducing kernel interpolant via multiple wavelet expansion. accepted, Comput. Mech
Li S, Liu WK (1997b) Moving least-square reproducing kernel method (III): wavelet packet &its applications. submitted, Comput. Meth. Appl. Mech. Eng
Liu WK, Chang H, Chen JS, Belytschko T (1988) Arbitrary Lagrangian Eulerian Petrov-Galerkin finite elements for nonlinear continua. Comp. Meth. Appl. Mech. Eng. 68:259–310
Liu WK, Chen JS, Belytschko B, Zhang YF (1991) Adaptive ALE finite elements with particular reference to external work rate on frictional interface. Comp. Meth. Appl. Mech. Eng. 93:189–216
Liu WK, Hu Y.-K, Belytschko B (1992) ALE finite elements with hydrodynamic lubrication for metal forming. Nucl. Eng. Des. 138:1–26
Liu WK, Oberste-Brandenburg C (1993) Reproducing kernel and wavelet particle methods. Aerospace structures: nonlinear dynamics and system response, eds. J. P. Cusumano, C. Pierre, S. T. Wu, AD33, ASME, 39–56
Liu WK, Jun S, Li S, Adee J, Belytschko B (1995a) Reproducing kernel particle methods for structural dynamics. Int. J. Numer. Meth. Eng. 38:1655–1679
Liu WK, Chen Y (1995b) Wavelet and multiple scale reproducing kernel particle methods. Int. J. Numer. Meth. Fluids 21:901–931
Liu WK, Jun S, Zhang YF (1995c) Reproducing kernel particle methods. Int. J. Numer. Meth. Fluids 20:1081–1106
Liu WK, Chen Y, Jun S, Chen JS, Belytschko T, Pan C, Uras RA, Chang CT (1996a) Overview and applications of the reproducing kernel particle methods. Arch. Comput. Meth. Eng. State Art Rev. 3:3–80
Liu WK, Chen Y, Uras RA, Chang CT (1996b) Generalized multiple scale reproducing kernel particle methods. Comput. Meth. Appl. Mech. Eng. 139:91–157
Liu WK, Chen Y, Chang CT, Belytschko T (1996c) Advances in multiple scale kernel particle methods. Comput. Mech. 18:73–111
Liu WK, Li S, Belytschko T (1996d) Moving least square kernel galerkin method (I) methodology and convergence. in press, Comput. Meth. Appl. Mech. Eng
Lu YY, Belytschko T, Gu L (1994) A new implementation of the element free galerkin method. Comput. Meth. Appl. Mech. Eng. 113:397–414
Lucy L (1977) A numerical approach to testing the fission hypothesis.Astron. J. 8 (12):1013–1024
Male AT, Cockcroft MG (1965) A method for the determination of the coefficient of friction of metals under conditions of bulk plastic deformation. J. Inst. Metals 93:38–46
Melenk JM, Babuska I (1996) The partition of unity finite element method: basic theory and applications. Comput. Meth. Appl. Mech. Eng. 139:289–314
Monaghan JJ (1982) Why particle methods work. SIAM J. Sci. Stat. Comput. 3 (4):422–433
Monaghan JJ (1988) An introduction to SPH. Comp. Phys. Commun. 48:89–96
Nakamachi E, Sowerby R (1988) Finite element modeling of the punch stretching of square plates. J. Appl. Mech. 55:667–671
Nayroles B, Touzot G, Villon P (1992) Generalizing the finite element method: diffuse approximation and diffuse elements. Comput. Mech. 10:307–318
Oh SI, Kobayashi S (1980) Finite element analysis of plane-strain sheet bending. Int. J. Mech. Sci. 22:583–594
Reed WK, Atluri SN (1985) Constitutive modeling and computational implementation in finite strain plasticity. Int. J. Plasticity, (Invited Paper in Honor of J. F. Bell's 70th Birthday) 1:63–87
Randles PW, Libersky LD (1996) Smoothed particle hydrodynamics: some recent improvements and applications. Comput. Meth. Appl. Mech. Eng. 139:375–408
Roque CMOL (1996) Application of the finite element method to the cold forging sequence design. master dissertation, State University of Campinas
Rubinstein R, Atluri SN (1983) Objectivity of incremental constitutive relations over finite time steps in computational finite deformation analysis. Comput. Meth. Appl. Mech. Eng. 36:277–290
Saleeb AF, Chen K, Chang TYP (1994) An effective two-dimensional frictional contact model for arbitrary curved geometry. Int. J. Numer. Meth. Eng. 37:1297–1321
Simo JC, Taylor RL (1985) Consistent tangent operators for rate-independent elasto-plasticity. Comput. Meth. Appl. Mech. Eng. 48:101–118
Simo JC (1988) A framework for finite strain elastoplasticity based on maximum plastic dissipation and multiplicative decomposition: part I. continuum formulation; part II. computational aspects. Comput. Meth. Appl. Mech. Eng. 66:199–219; 68: 1–31

Simo JC (1992) Algorithms for static and dynamic multiplicative plasticity that preserve the classical return mapping schemes of the infinitesimal theory. Comput. Meth. Appl. Mech. Eng. 99:61–112
Wang NM, Budiansky B (1978) Analysis of sheet metal stamping by a finite element method. J. Appl. Mech. 45:73–82
Wifi AS (1976) An incremental complete solution of the stretch forming and deep drawing of a circular blank using a hemispherical punch. Int. J. Mech. Sci. 18:23–31
Zienkiewicz OC, Godbole PN (1974) Flow of plastic and viscoplastic solids with special reference to extrusion and forming processes. Int. J. Numer. Meth. Eng. 8:3–16
Zienkiewicz OC (1984) Flow formulation for numerical solution of forming processes. in numerical analysis of forming processes, JFT Pittman, OC Zienkiewicz, RD Wood and JM Alexander, eds, John Wiley & Sons, New York, pp 1–44